RESEARCH ARTICLE

Key Points:
- Community Integrated Earth System Model (CIESM) includes many new developments and modifications
- Preindustrial control and historical simulations were performed and evaluated
- Some persistent climate model biases are alleviated, but sea ice is significantly underestimated in the warm season

Supporting Information:
- Supporting Information S1

Correspondence to:
Y. Lin,
yanluan@tsinghua.edu.cn

Community Integrated Earth System Model (CIESM): Description and Evaluation

Yanluan Lin[1] [iD], Xiaomeng Huang[1] [iD], Yishuang Liang[1] [iD], Yi Qin[1] [iD], Shiming Xu[1] [iD], Wenyu Huang[1] [iD], Fanghua Xu[1] [iD], Li Liu[1] [iD], Yong Wang[1] [iD], Yiran Peng[1] [iD], Lanning Wang[2], Wei Xue[1], Haohuan Fu[1], Guang Jun Zhang[3], Bin Wang[1,4] [iD], Ruizhe Li[1], Cheng Zhang[1], Hui Lu[1] [iD], Kun Yang[1] [iD], Yong Luo[1], Yuqi Bai[1] [iD], Zhenya Song[5] [iD], Minqi Wang[1] [iD], Wenjie Zhao[1], Feng Zhang[6] [iD], Jingheng Xu[1], Xi Zhao[1], Chunsong Lu[6], Yizhao Chen[7] [iD], Yiqi Luo[8] [iD], Yong Hu[1], Qiang Tang[1], Dexun Chen[9], Guangwen Yang[10], and Peng Gong[1] [iD]

[1]Department of Earth System Science/Ministry of Education Key Laboratory for Earth System Modeling, Tsinghua University, Beijing, China, [2]College of Global Change and Earth System Science, Beijing Normal University, Beijing, China, [3]Scripps Institution of Oceanography, La Jolla, California, USA, [4]Institute of Atmospheric Physics, Chinese Academy of Sciences, Beijing, China, [5]First Institute of Oceanography, Ministry of Natural Resources, Qingdao, China, [6]Department of Atmospheric and Oceanic Sciences & Institute of Atmospheric Sciences, Fudan University, Shanghai, China, [7]Joint Innovation Center for Modern Forestry Studies, College of Biology and the Environment, Nanjing Forestry University, Nanjing, China, [8]Center for Ecosystem Science and Society, Department of Biological Sciences, Northern Arizona University, Flagstaff, AZ, USA, [9]Jiangnan Institute of Computing Technology, Wuxi, China, [10]National Supercomputing Center in Wuxi, Wuxi, China

Abstract A team effort to develop a Community Integrated Earth System Model (CIESM) was initiated in China in 2012. The model was based on NCAR Community Earth System Model (Version 1.2.1) with several novel developments and modifications aimed to overcome some persistent systematic biases, such as the double Intertropical Convergence Zone problem and underestimated marine boundary layer clouds. Aerosols' direct and indirect effects are prescribed using the MACv2-SP approach and data sets. The spin-up of a 500-year preindustrial simulation and three historical simulations are described and evaluated. Prominent improvements include alleviated double Intertropical Convergence Zone problem, increased marine boundary layer clouds, and better El Niño Southern Oscillation amplitude and periods. One deficiency of the model is the significantly underestimated Arctic and Antarctic sea ice in warm seasons. The historical warming is about 0.55 °C greater than observations toward 2014. CIESM has an equilibrium climate sensitivity of 5.67 K, mainly resulted from increased positive shortwave cloud feedback. Our efforts on porting and redesigning CIESM for the heterogeneous Sunway TaihuLight supercomputer are also introduced, including some ongoing developments toward a future version of the model.

Plain Language Summary Based on NCAR Community Earth System Model (Version 1.2.1), a Community Integrated Earth System Model was introduced. It has over 10 major modifications and developments aimed to reduce some persistent biases in Community Earth System Model Version 1.2.1. Evaluation of simulations for Coupled Model Intercomparison Project Phase 6 indicated that the model produced reasonable mean climate states with improvement in rainfall, cloud, and El Niño Southern Oscillation. Community Integrated Earth System Model has an equilibrium climate sensitivity of 5.67 K, much higher than all CMIP5 models. Some of the deficiencies of the model, such as the underestimated Arctic and Antarctic sea ice in warm seasons and the greater warming in the early 21st century, will be investigated in the future.

1. Introduction

Earth system model (ESM) has become a powerful tool for the understanding of the complex Earth climate system and the projection of future warming due to increased greenhouse gas emissions (Flato et al., 2013). However, despite the extensive improvement of ESM, there still remain various systematic biases. These include, but not limited to, double intertropical convergence zones (ITCZ), weak intraseasonal oscillation such as Madden Julian Oscillation, and underestimated marine boundary layer clouds (Kay et al., 2016; Zadra et al., 2018; M. Zhang et al., 2018). Biases resulting from air-sea coupling also remain in most

models. For example, model-simulated El Niño Southern Oscillation (ENSO) period has been too regular with overestimated amplitudes (Gent et al., 2010). ENSO simulation gradually improved with continuous model development at NCAR (Danabasoglu et al., 2020; Deser et al., 2012; Neale et al., 2008). Decadal variabilities, such as Pacific Decadal Oscillation and Atlantic Meridional Overturning Circulation (AMOC), are still hard to be well captured, not to mention useful predictions. These systematic biases significantly influence our confidence in the projection capability of various models, especially for regional climate changes. Accordingly, the origins and consequences of systematic model biases have been listed as one of the three broad scientific questions of Coupled Model Intercomparison Project Phase 6 (CMIP6) (Eyring et al., 2016; Lin et al., 2017).

Tsinghua University has decided to develop an ESM back in 2009. Instead of starting from scratch, the development strategy was set to overcome those remaining systematic biases in current models. We chose to base the model development on the state-of-the-art Community ESM of the National Center for Atmospheric Research (NCAR, CESM1.2.1; Hurrell et al., 2013) but with various independent developments from there. In collaboration with other research institutions and universities in China, new process level physics, model components, grid mesh designs, and dynamic cores will be gradually included as they are ready. Due to its collaborative nature among different institutions and our intention to make it openly available to the community, the model is named Community Integrated ESM (CIESM) to pay tribute to CESM. As a first step, we intended to participate in CMIP6 (Eyring et al., 2016) using the first version of CIESM, which included various developments as described later. This version for the CMIP6 participation will not include terrestrial and ocean biogeochemical processes and carbon cycles and is thus essentially a Climate System Model. In the near future, more model modifications will be included. At the same time, model resolutions will be gradually increased with better parallel computing performance tailored to the new supercomputer architecture designed in China.

A significant amount of effort has been put into ESM development efforts in China since CMIP3. For example, while five models from China participated in CMIP5 (Zhou et al., 2014), for the upcoming CMIP6, nine models from China have planned on participating in CMIP6 (Zhou et al., 2020). This will provide model diversity and an opportunity for more in-depth intercomparison among these models, as well as more communications and collaborations among modeling centers. This will facilitate the progress of ESM development and expedite Earth system science research in China. Progress of model development in China and some brief introduction of these models can be found in Cao et al. (2018) and Zhou et al. (2014, 2020).

The paper is organized as follows: An overview of the model development and porting to a new computing architecture is provided in section 2. Model tuning and experiment design are introduced in section 3. Diagnostic, Evaluation, and Characterization of Klima (DECK) simulation results, including a 500-year preindustrial coupled simulation and three historical simulations, are described and evaluated in section 4. Conclusions are summarized in section 5 with a brief introduction of ongoing developments and future plan.

2. Overview of the CIESM Development Efforts

CIESM is developed based on NCAR CESM1.2.1 (called CESM1 hereafter), which is a comprehensive, state-of-the-art ESM in the world. More details about the CESM can be found in a series of papers (Danabasoglu et al., 2012; Hurrell et al., 2013) with detailed documents describing the model components (Neale et al., 2012). We will focus on the modifications we have made to improve the model performance with a specific goal to overcome and alleviate some of the persistent systematic biases in CESM1. Table 1 summarized all the major modifications used in the model for the CMIP6 simulations.

2.1. Atmospheric Model Development

The atmospheric model development is based on the Community Atmospheric Model Version 5 (CAM5; Neale et al., 2012). We have worked on the finite volume dynamic core during the development stage but chose to use the spectral element dynamics core (Lauritzen et al., 2014) with an approximately 1° resolution in consideration of available computing resource for the model integration. The model has 30 hybrid levels in the vertical with the model top at 1 hPa.

The atmospheric development is mainly focused on a few key physical processes critical to alleviation of some systematic biases in CESM1, such as the marine boundary layer clouds and the double ITCZ

Table 1
Modifications Used in the CIESM and Comparison With CESM1.2.1

Modifications	CIESM1.1	CESM1.2.1
Deep convection	Modified ZM scheme including stochasticity and convective microphysics (Song & Zhang, 2011; Wang et al., 2016)	ZM scheme (Neale et al., 2012; G. J. Zhang & McFarlane, 1995)
Cloud macrophysics including cloud fraction and condensation	PDF cloud scheme (Qin et al., 2018)	M. Zhang et al. (2003) and Park scheme (S. Park et al., 2014)
Cloud microphysics	Single-ice scheme (Zhao et al., 2017)	GM1.5 (Gettelman et al., 2008)
Shortwave radiation	Four-stream shortwave radiation (F. Zhang & Li, 2013)	Two-stream correlated-k distribution Rapid Radiation Transfer Model (Iacono et al., 2008)
Orographic form drag	BBW04 scheme (Liang et al., 2017)	Turbulent Mountain Stress scheme (Neale et al., 2012)
Aerosol	MACv2-SP (Stevens et al., 2017)	Interactive aerosols (Liu et al., 2012)
Tidal mixing	Slightly enhanced energy flux due to the barotropic tide around the Maritime Continent	Abyssal tidal mixing (Danabasoglu et al., 2012)
Ocean surface albedo	Solar zenith angle and 10-m wind speed dependent (Jin et al., 2011)	Fixed
Soil data	Global Soil Dataset for use in Earth System Models (Wei et al., 2014)	International Geosphere-Biosphere Programme soil data set (IGBP, 2000)
Thermal roughness length parameterization	A new thermal roughness length parameterization (Yang et al., 2008)	Zeng and Dickinson (1998) and Neale et al. (2012)
Sea ice lateral melting rate	Sea ice concentration dependent floe length (Lüpkes et al., 2012)	A constant value of 300 m for sea ice floe size
Coupler	C-Coupler2 (Liu et al., 2014, 2018)	Coupler 7
Running machine	Sunway TaihuLight (Fu et al., 2016)	Intel-based computer

Note. Please see the text for more details.

problem. Note that these biases have been alleviated in CESM2 via different model modifications (Danabasoglu et al., 2020). To alleviate these biases, the default cumulus parameterization scheme is heavily modified, the cloud macrophysics scheme (S. Park et al., 2014) is replaced by a diagnostic statistical cloud scheme, a simplified single ice cloud microphysics is developed, and a four-stream shortwave radiation calculation is included.

2.1.1. Convective Parameterization Modifications

The convective parameterization scheme in CIESM is based on the ZM scheme (G. J. Zhang & McFarlane, 1995) with two major modifications: a stochastic parameterization for convection (Plant & Craig, 2008; Wang et al., 2016) and the convective microphysics scheme of Song and Zhang (2011). As GCM resolution increases, the stochasticity of convection becomes important and must be accounted for. In this configuration, the expected mean convective activity (as measured by cloud base mass flux) at a given time and grid point is determined by the closure condition of the ZM scheme, but the deviation of the actual realization from the mean is governed by the stochastic parameterization of Plant and Craig (2008). They found that even at relatively coarse resolution, accounting for convective stochasticity can significantly improve the simulated characteristics of precipitation. The treatment of microphysical processes inside convective updrafts is simplistic with a tuning parameter used to account for all of the complex microphysical processes in the conversion of cloud condensates to precipitation in the default ZM scheme. Song and Zhang (2011) introduced a comprehensive two-moment convective microphysics scheme to the ZM scheme, in which both mass and number concentrations of cloud hydrometeor species (cloud water, cloud ice, rainwater, and snow) are obtained diagnostically. The microphysical processes considered in the parameterization include autoconversion, self-collection, collection between hydrometeor species, freezing, cloud ice nucleation, droplet activation, and sedimentation. Simulations using the NCAR CAM5 show that the convective microphysics scheme improves the vertical distribution of cloud properties and cloud radiative forcing (Song et al., 2012; Storer et al., 2015).

2.1.2. PDF Cloud Macrophysics

Marine boundary layer clouds are still underestimated in CAM5 and CESM1 (Kay et al., 2016). As a result, too much shortwave radiation reaches the eastern basin of oceans and results in positive SST bias there. Cloud macrophysics in CAM5 includes a relative humidity cloud fraction following S. Park et al. (2014) and the condensation scheme of M. Zhang et al. (2003). Due to various condensate sources, such as

convective detrainment, there are a total of four types of cloud fractions in CAM5 (Neale et al., 2012; S. Park et al., 2014). As a result, inconsistency between cloud fraction and cloud condensate occurs frequently, and adjustment between the two is needed (S. Park et al., 2014).

A new statistical PDF cloud scheme, assuming a Gaussian distribution for a combined variable (called s) of total water and liquid water potential temperature, was developed (Qin et al., 2018). The approach diagnoses the subgrid-scale variance of s from the boundary layer mixing scheme (Bretherton & Park, 2009) and shallow convection scheme (S. Park & Bretherton, 2009) in CAM5. As a result, the scheme is able to capture the spatially and temporally varying subgrid-scale variances and capture the distribution of marine low clouds better, especially over regions dominated by stratocumulus and trade wind cumulus. The scheme also helps alleviate the double ITCZ problem in CESM1.2.1 (Qin & Lin, 2018), and its impact in CIESM is similar as shown later.

2.1.3. A Single Ice Microphysics

Based on the two-moment microphysical parameterization (Gettelman et al., 2008; Morrison & Gettelman, 2008), a modified microphysical scheme combining cloud ice and snow into a single prognostic variable (called total ice) has been developed (Zhao et al., 2017). In the new approach, riming and temperature impacts on ice particle properties, such as their area, mass, and fall velocity, are included following Lin and Colle (2011) and Lin et al. (2011). The new approach not only reduces the computational time because several ice-phase and mixed-phase microphysical processes are no longer needed but also is more physically based because empirical conversion from ice to snow is no longer needed. Modeled ice water content, liquid water content, and cloud top height distribution are improved. Due to its simplified representation of microphysical processes and flexible description of ice particle properties, the single-ice approach is a promising direction for future GCM microphysics development.

2.1.4. Four-Stream Shortwave Radiation Calculations

The shortwave radiative module of CAM5 uses the two-stream correlated-k distribution Rapid Radiation Transfer Model (Iacono et al., 2008). A four-stream spherical harmonic expansion approximation (Li & Ramaswamy, 1996; F. Zhang & Li, 2013) is applied in the current model to replace the default two-stream scheme for shortwave radiative calculation. The computational expense for the new scheme is slightly higher than the default one. The scheme reduces the error of radiative fluxes comparing to the two-stream scheme, especially at large solar zenith angels when aerosol or clouds with thin optical depth are present. Global model simulations indicated that the scheme improved the shortwave cloud forcing (SWCF) over midlatitude oceans and aerosol direct radiative forcing over desert areas (H. Zhang et al., 2015).

2.1.5. Parameterization of Subgrid-Scale Orographic Form Drag

Subgrid orographic turbulent drag has significant effects on the atmosphere motion. A Turbulent Mountain Stress scheme, which represents turbulent drag as a drag coefficient to calculate the momentum flux in the surface layer and influences the wind profiles in the upper layers through vertical diffusion process, is used in CAM5. Following Beljaars et al. (2004), we included turbulent drag as a direct term in the dynamic equation of atmospheric motion (Liang et al., 2017). The new method is more sensitive to complex orography and improves low-level wind speed over complex orography.

2.1.6. Prescribed Aerosol Forcing

Due to the different representation of aerosol direct and indirect radiative forcing in climate models, large discrepancies of aerosol impact on simulated climate have been diagnosed (e.g., Myhre et al., 2013). In order to reduce the uncertainty brought by aerosol effects on climate simulations, we follow the approach proposed by CMIP6 using the aerosol forcing data set MACv2-SP (the second version of the Max Planck Institute Aerosol Climatology). MACv2-SP provides prescribed increments of anthropogenic aerosol optical properties (i.e., the direct aerosol effect) and the first indirect aerosol effect over the historical period (1850–2016), relative to their preindustrial counterparts simulated in Year 1850 (Stevens et al., 2017). First, the anthropogenic aerosol extinction, asymmetry factor, and single-scattering albedo at 550 nm given in the climatology data set and scaled to different shortwave wavelength bands with the spectral-dependent information are applied in the radiative transfer scheme of the model. The longwave effect of anthropogenic aerosols is small and not considered. Second, MACv2-SP data set provides the increments of droplet number concentration caused by the anthropogenic aerosols for stratiform clouds. With this, we diagnose the slope and shape parameter of the gamma distribution of cloud droplet size distribution in the cloud microphysical scheme. The impacts on cloud albedo are accounted for in the

radiative transfer scheme to obtain the aerosol indirect effect on cloud optical properties. Additionally, the stratospheric aerosol forcing (mainly caused by volcano eruptions) is prescribed at multiple vertical levels in the stratosphere for the historical period following the CMIP6 procedure (Thomason, 2012). Data near the tropopause are interpolated to smooth the transition of aerosol properties between the stratosphere and troposphere. The provided stratospheric aerosol data are fit to the shortwave bands of the radiative transfer scheme in the model.

2.2. Ocean Model Development

The ocean model is based on LANL Parallel Ocean Program Version 2 (POP2; Smith et al., 2010), which uses a nominal grid of 1° with the North Pole displaced to Greenland. There were several modifications of model physics to improve the model overall simulations (Danabasoglu et al., 2012). We have done some modifications to the default POP2, including a more efficient barotropic solver, modified tidal mixing, and a new air-sea flux exchange method.

2.2.1. An Efficient Barotropic Solver

Time-splitting method was adopted in many ocean models, such as POP2, to overcome the severe limitation on the length of time step. The separated barotropic mode is solved as a 2-D elliptic system. Conjugate Gradient algorithm and its variants are widely used to solve this elliptic system previously. However, with increased resolution, the barotropic solver based on these algorithms becomes a major bottleneck because of inherent shortage of these algorithms in the global reduction operation. A new barotropic Solver, named Preconditioned Classical Stiefel Iteration, is designed to avoid the global reduction operations and reduce the number of iterations per time step to improve the parallel performance in the high-resolution simulation. Preconditioned Classical Stiefel Iteration includes a classical Stiefel iteration algorithm and an effective block Error Vector Propagation preconditioner. More details can be found in Hu et al. (2013, 2015) and X. Huang et al. (2016). This new barotropic solver with block Error Vector Propagation preconditioner can accelerate the ocean simulation in 0.25° from 6.2 simulated years per day wallclock (SYPD) to 10.5 SYPD on 16,875 parallel cores. With its much-improved computational efficiency, the method has been adopted in CESM2 (Danabasoglu et al., 2020).

2.2.2. Modified Ocean Tidal Mixing

Tidal mixing plays an important role in providing mechanical energy for the global ocean circulation (Brierley & Fedorov, 2011). In the default POP2, tidal mixing is treated as a function of the energy flux out of the barotropic tide. However, as shown by Schmittner and Egbert (2014), the total energy flux out of the barotropic tide used in the ocean model is remarkably reduced (0.5–1 TW) compared to that estimated from the satellite altimetry (~3.3 TW) or the tide model (~3.5 TW). This underestimation in the energy flux is partially due to the coarser resolution of the ocean model. In particular, the oceans surrounding the Maritime Continent severely suffered from this underestimation (Schmittner & Egbert, 2014). Therefore, we have slightly enhanced the energy flux due to the barotropic tide around the Maritime Continent. This modification strengthens the tidal mixing around the Maritime Continent and reduces the SST warm bias there, which further gives rise to a more realistic zonal pressure gradient in the tropical Pacific and improves the simulation of ENSO.

2.2.3. A Modified Air-Sea Flux Parameterization

Previous studies found that wind stress is modified over regions with large SST gradients (e.g., Chelton et al., 2004; Chelton & Xie, 2010; K.-A. Park et al., 2006; Small et al., 2008; R.-H. Zhang et al., 2014). Due to the low resolution in current POP2, SST fronts simulated will be smoothed out, and thus, the effect of SST gradient on wind stress might be underestimated. Following Hogg et al. (2009), a correction term to the relative velocity between ocean surface currents and 10-m wind ($\left|\Delta\overrightarrow{U}\right|$) is applied, $\left.\left|\Delta\overrightarrow{U}\right|\right|_{\text{new}} = (1 + \alpha(T_o - T_a))\left|\Delta\overrightarrow{U}\right|$, where α is the coupling coefficient parameter to represent the strength of wind stress feedback. The wind stress is then updated as $\overrightarrow{\tau}_s = \rho C_D \left.\left|\Delta\overrightarrow{U}\right|\right|_{\text{new}} \Delta\overrightarrow{U}$, and surface latent heat flux and sensible heat flux are changed accordingly. With the updated surface heat flux and wind stress, the simulation of equatorial Pacific current system is improved with reduced global SST biases (F. Xu, 2018). The overestimated ENSO magnitude in the original CESM is reduced by ~30% after using the new scheme with an improved period.

2.2.4. A Wind Speed-Dependent Sea Surface Albedo

Ocean surface albedo has significant effects on radiation budget at the atmosphere-ocean boundary. The roughness introduced by surface wind stresses has great influences on the direct and diffuse albedo at sea surface (Payne, 1972; Preisendorfer & Mobley, 1986). CIESM applied an algorithm taking the low-level wind speed into account for the calculation of direct and diffuse albedo for visible and near-infrared radiations at sea surface in the coupler directly. Following Jin et al. (2011), the direct and diffuse albedo is a function of solar zenith angle and 10-m wind speed.

2.3. Land Surface Model Development

In CIESM, two modifications have been implemented in the land surface model (CLM4.0; Lawrence et al., 2011), that is, adoption of a newly released global soil data and an improved thermal roughness parameterization.

2.3.1. New Soil Texture and Organic Matter Content Data

Soil properties are essential to the performance of land surface model. The land surface water and energy budgets are controlled by the soil thermal and hydrological parameters, which in turn are determined by the soil texture and organic matter content. Recently, Beijing Normal University released a Global Soil Dataset for use in ESMs (GSDE; Wei et al., 2014), which merges soil map of the world and regional soil maps. In the revised CLM4.0, soil parameters from GSDE are used to provide soil texture and organic content information of eight layers from the surface to the depth of 2.3 m. In general, GSDE has lower soil organic content, especially in high latitude regions of the Northern Hemisphere and most parts of China (not shown). Such changes will impact land surface heat and water flux, in which organic matter plays important roles. Moreover, the spatial variation of GSDE is larger than the default data in CLM4.0, which means the values in GSDE is more heterogeneous in space than the latter.

2.3.2. A New Thermal Roughness Length Parameterization

Arid and semiarid region covers around 60% of global land surface. Land covers in these regions are mainly sparse vegetation. Meanwhile, these regions are sensitive to climate change due to their vulnerable ecological system. In CIESM, in order to improve the performance of land surface heat budget modeling in these regions, we adopt a new thermal roughness length scheme proposed by Yang et al. (2002, 2008) to improve the sensible heat flux and land surface energy budget. Test of the scheme in the Noah LSM suggested that simulated land surface temperature was improved relative to the original scheme (Chen et al., 2011).

2.4. Sea Ice Model Development

The sea ice model in CIESM is based on Community Ice CodE Version 4.1 with a few modifications to the sea ice physics and dynamics. The sea ice model has the same grid structure as the ocean model as described before. The freezing temperature in the original POP and CICE is set as a constant at −1.8°C. In contrast, the freezing temperature of sea ice is related to the salinity of seawater in the CIESM, with an algorithm to consider the linear relationship between salinity and freezing temperature.

A diagnostic floe size parameterization is added to the sea ice component of CIESM. By utilizing in situ measurements in the Arctic and Antarctic, the typical floe length is diagnosed using the prognostic sea ice concentration, with differentiation between the two polar regions (Lu et al., 2008; Lüpkes et al., 2012). The floe length is then used to compute the lateral melting rate (Tsamados et al., 2015). With this parameterization, the floe size in the sea ice component is effectively reduced in marginal ice zones and attains better matching with observations. Compared with the constant value of 300 m for sea ice floe size in the default sea ice component, this new scheme improves the lateral melting rates in sea ice edges, which is an important melting process especially for the Antarctic but not well characterized in previous models.

2.5. Coupling Architecture

Community Coupler Version 2 (C-Coupler2; Liu et al., 2018), the next version of C-Coupler1 (Liu et al., 2014), is employed in CIESM to handle the fundamental model coupling functions, that is, data transfer and data interpolation, which are handled by the Model Coupling Toolkit (Larson et al., 2005) in CESM1.2.1, while the driver of CESM1.2.1 (Craig et al., 2012) is still retained for flexible processor layout between the component models for better parallel performance. It is demonstrated that C-Coupler2 can achieve bitwise identical simulation results with Model Coupling Toolkit. With the employment of C-Coupler2, the coupling architecture of CIESM is upgraded with the new features of C-Coupler2, that is, capability of model

coupling within one executable or among different executables, dynamic 3-D coupling, nonblocking data transfer, flexible and automatic coupling generations, and facilitation for incremental coupling. For example, C-Coupler2 can couple an external model (a component model or a coupled model) with CIESM, where two sets of executables will be generated (one for the external model and the other for CIESM) with minimal modifications required to the drivers of the models.

2.6. Porting the Model to TaihuLight Supercomputer

To better utilize the fast-growing supercomputer in China, we have modified the model codes significantly to facilitate its simulation in new computer architectures, such as supercomputer Sunway TaihuLight at National Supercomputing Center in Wuxi, China. Each core group (CG) on TaihuLight is composed of one management processing element and 64 computing processing elements. It has a peak performance over 125 PFlops, with the Linpack performance of over 93 Plops (Fu et al., 2016). The architectural differences between the Sunway machine and previous Intel machines bring challenges for programming. Therefore, it is becoming extremely difficult for well-established numerical codes, such as the million lines of code in the climate domain, to gain performance benefits, if any, from the newly built supercomputers. Extensive refactor and redesign work have been conducted for both the dynamical core and the physics schemes in the atmospheric and ocean model of the CIESM at this stage.

We used OpenACC-based refactoring as the major approach and applied source-to-source translator tools to exploit the most suitable parallelism for Sunway TaihuLight and to fit the intermediate variable into the limited on-chip fast buffer. Combining the OpenACC-refactored code with the projected performance upper bound based on the memory capacities (assuming bandwidth as the major constraint), we then derived a more aggressive fine-grained optimization workflow that maps the original OpenACC directive description of parallelism into a more flexible Athread code, to enable finer memory control and more efficient vectorization.

After the porting and optimization, the simulation speed of the atmosphere component improves from 14.21 SYPD to 23.67 SYPD using 5,400 MPI processes for a resolution of 100 km (ne30 configuration). For a higher resolution of 25 km (ne120 configuration), the simulation speed of the atmosphere component improves from 1.30 SYPD to 2.48 SYPD using 14,400 MPI processes. To demonstrate the extreme level of performance that can be achieved on Sunway TaihuLight, further fine-grained optimization for the CAM-SE dynamical core part manages to scale to 10,075,000 cores for a 750-m global atmospheric simulation and provides an unprecedented performance of 3.3 PFlops with double precision. The coupled simulation was run using 5,400 CGs for the atmosphere, land, sea ice, coupler component, paralleled with 960 CGs for the ocean component. The coupled model performance averages 10 SYPD.

3. Tuning and Experimental Design

All of the CIESM development work was conducted and tested on an Intel-based machine first. Different developments were carried out separately by individuals in general. The strategy is to put all the finished modifications together for a final tuning based on coupled simulations at an agreed time.

Tuning is a critical step in climate model development (Hourdin et al., 2017). Due to the time constraint, most of the tuning aims to reduce the TOA imbalance to less than 0.5 W m^{-2} in long-term preindustrial (piControl) simulations. Although we have paid attention to the model TOA radiation balance for some of the modifications introduced during the development stage, such as the PDF cloud macrophysics and single-ice microphysics, the model is out of radiation balance (4 W m^{-2}) when all the modifications (Table 1) are put together for the first time in the coupled simulation. Tuning parameters include the RH threshold for high cloud fraction, entrainment rate, and rain evaporation efficiency of the ZM scheme. After a series of tuning efforts, we are able to achieve a TOA radiation balance (<0.1 W m^{-2}) on an Intel-based supercomputer.

However, the supercomputer we are planning to use for the CMIP6 experiment integration is the Sunway TaihuLight supercomputer, which used a different computing architecture. To better utilize the supercomputer, we chose to use the spectral element dynamic core instead of the finite volume used during the development stage. This brought some impacts on the model results. For example, we cannot obtain a similar TOA radiation balance after the porting to the new supercomputer. This means a retuning of the model.
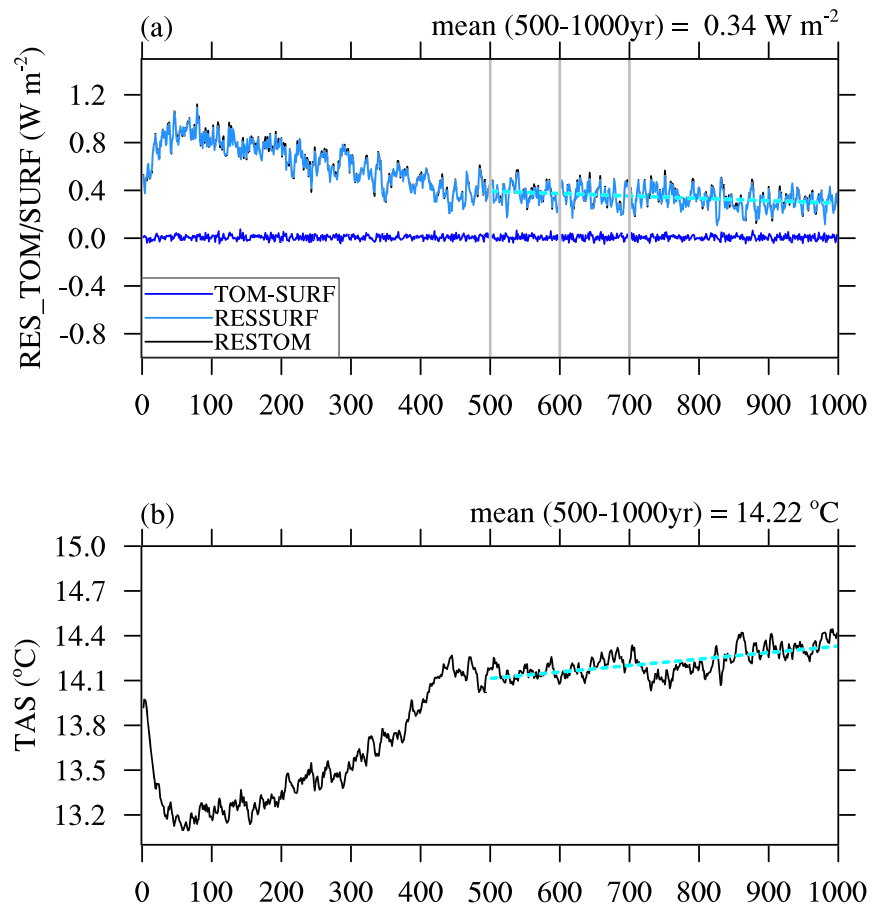
Figure 1. Time series of TOA and surface radiative fluxes (a) and global mean surface air temperature (b) for the 1,000-year piControl simulation. The fitting line shows the linear trend for the piControl simulation (Years 501–1,000). The three vertical lines in (a) indicate the starting time of the three historical simulations.

After a series of tuning efforts, we were able to reduce the global mean radiation imbalance to ~0.34 W m^{-2} with a global mean surface temperature drift <0.04°C per century after 500 years of spin-up in the piControl simulation (Figure 1). Although this is not optimal, it is acceptable given the computing resources and time constraint. We note that some CMIP6 models also have similar magnitudes of drift.

The piControl integration was initialized at a cold start in 1850 with prescribed greenhouse gas concentration, aerosol, and other external forcing as required by CMIP6 (Eyring et al., 2016). The initial atmospheric and aerosol-related flux data for the atmospheric model are the climatological data in 1850 produced by one realization from CESM1.2.1. The background volcanic aerosol was prescribed based on the average during the historical simulation (1850–2014). The ocean model was initialized using the Polar science center Hydrographic Climatology data. Other configurations followed the CMIP6 specifications and forcings. The evolution of annual global mean TOA and surface net radiative flux and surface air temperature for the spin-up and simulation of piControl are shown in Figure 1. Surface net flux is basically identical to the TOA flux. This indicated that the atmosphere conserved total energy well as shown by a near-zero difference between the TOA and surface energy flux (Figure 1a). Initially, the simulation experienced a rapid cooling during the first 30 years (Figure 1b) probably resulted from the change of the forcing from present day to preindustrial. After that, the simulation showed a gradual warming until around Year 450 due to a net influx of energy at TOA. After that, the simulation approximately reached a quasi-steady state with the TOA net radiative imbalance stabilized at ~0.34 W m^{-2} and annual global mean surface air temperature of 14.22°C. There is still a slight warm drift (0.04°C per century) after Year 500, but we deem it acceptable and start the piControl simulation at Year 501. The simulation was continued for another 500 years, and
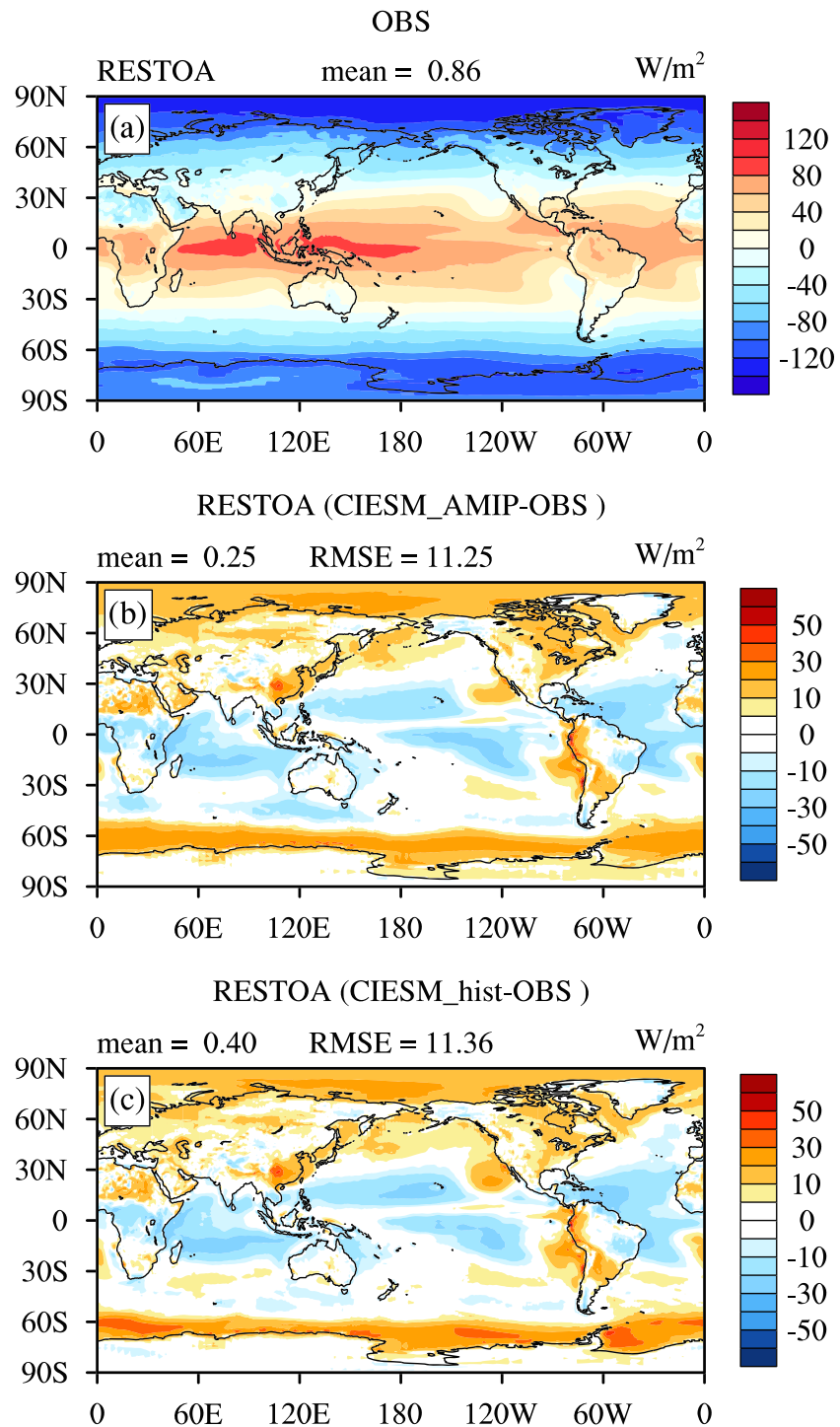
Figure 2. TOA net radiative fluxes from (a) CERES-EBAF (2001–2015), (b) differences between the CIESM AMIP simulation and CERES-EBAF, and (c) differences between the CIESM historical simulation and CERES-EBAF.

the simulation from 501–1,000 years is used for the later analysis. Although we expect that the model can be further integrated to reach a better equilibrium, computer resources and time constraint prohibited us to continue the integration at this stage.

All simulations adhere to the CMIP6 DECK specifications (Eyring et al., 2016) as closely as possible. The idealized 1% year^{-1} CO$_2$ increase (1pctCO$_2$) and abrupt CO$_2$ quadrupling (abrupt-4×CO$_2$) simulations
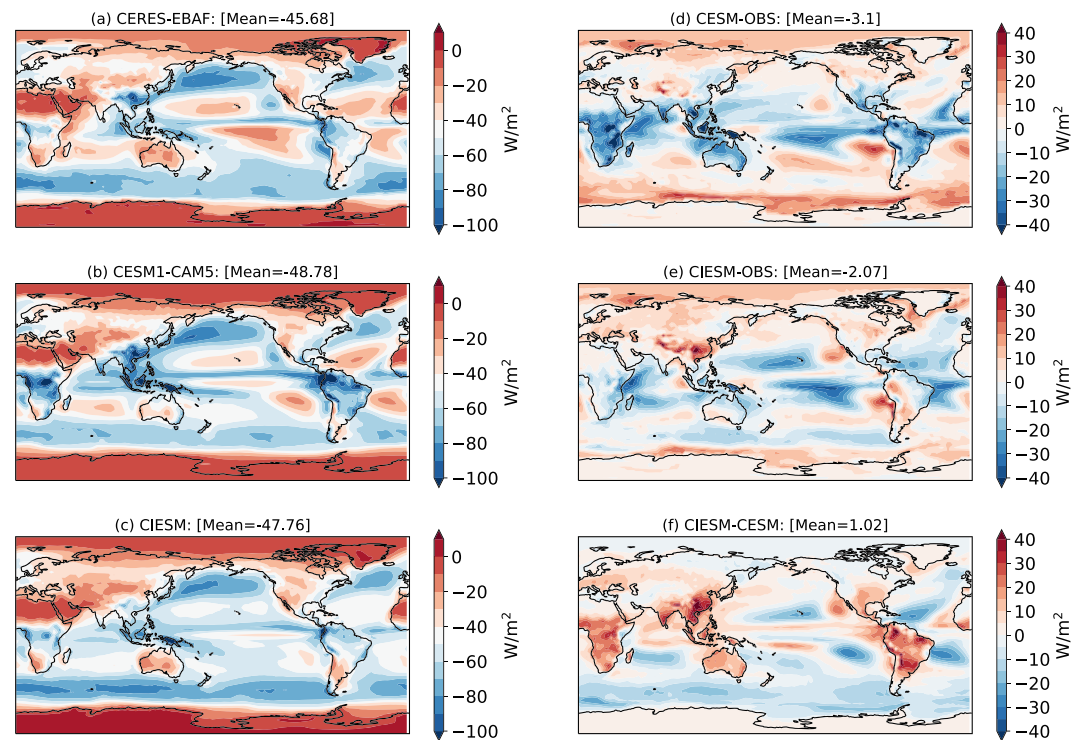
Figure 3. Annual mean SWCF of (a) CERES-EBAF, (b) CESM1, and (c) CIESM. (d) Bias of CESM1 relative to CERES-EBAF and (e) bias of CIESM relative to CERES-EBAF. (f) SWCF difference between CIESM and CESM1. Global mean value is also shown for each panel.

were branched from 1 January of Year 1 from the piControl. Similarly, the first historical simulation (historical_H1) was also branched from 1 January of Year 1 from the piControl. Subsequent two historical simulation members (historical_H2 and historical_H3) were branched every 100 years for a total of three ensemble members. We also conducted three Atmospheric Model Intercomparison Project (AMIP) historical simulations (1870–2014 using prescribed SST and sea ice) initialized from Year 1870 of the three historical simulations.

4. Model Evaluation

To compare with available observations, historical simulations (ensemble mean from the three coupled and AMIP simulations) from 1985–2014 are used for the present-day mean climatology evaluation. The present-day mean climatology is from 1981–2005 for CMIP5 models and CESM1. While for model internal variability, 500-year piControl simulation results are used. Finally, we evaluate the historical warming and climate sensitivity of the model.

4.1. Atmosphere Climatology

Annual mean TOA net radiation measured by CERES-EBAF is positive over the tropics with values up to 100 Wm^{-2} over regions dominated by deep convections and negative over higher latitudes (Figure 2a). The historical simulation has a global annual mean TOA net radiation of 1.26 Wm^{-2}, which is about 0.40 Wm^{-2} larger than that measured by CERES-EBAF (Figure 2c; 0.86 Wm^{-2} with an uncertainty range of 0.2 to 1.0 Wm^{-2}) (Wild et al., 2013). The imbalance is slightly larger than that in the piControl as discussed above. Compared to CERES-EBAF, the simulation gains less net flux of energy over the tropics (~7.5 Wm^{-2} in 20°N to 20°S) but receives more energy over the higher latitudes, especially over the Arctic and Southern Ocean. Such positive biases are mainly dominated by much larger (~50 Wm^{-2}) absorbed shortwave radiation than observed in the Arctic and Southern Ocean (south of 60°S) in JJA and DJF, respectively (supporting information Figure S1). About half of these positive biases came from clear sky shortwave flux bias
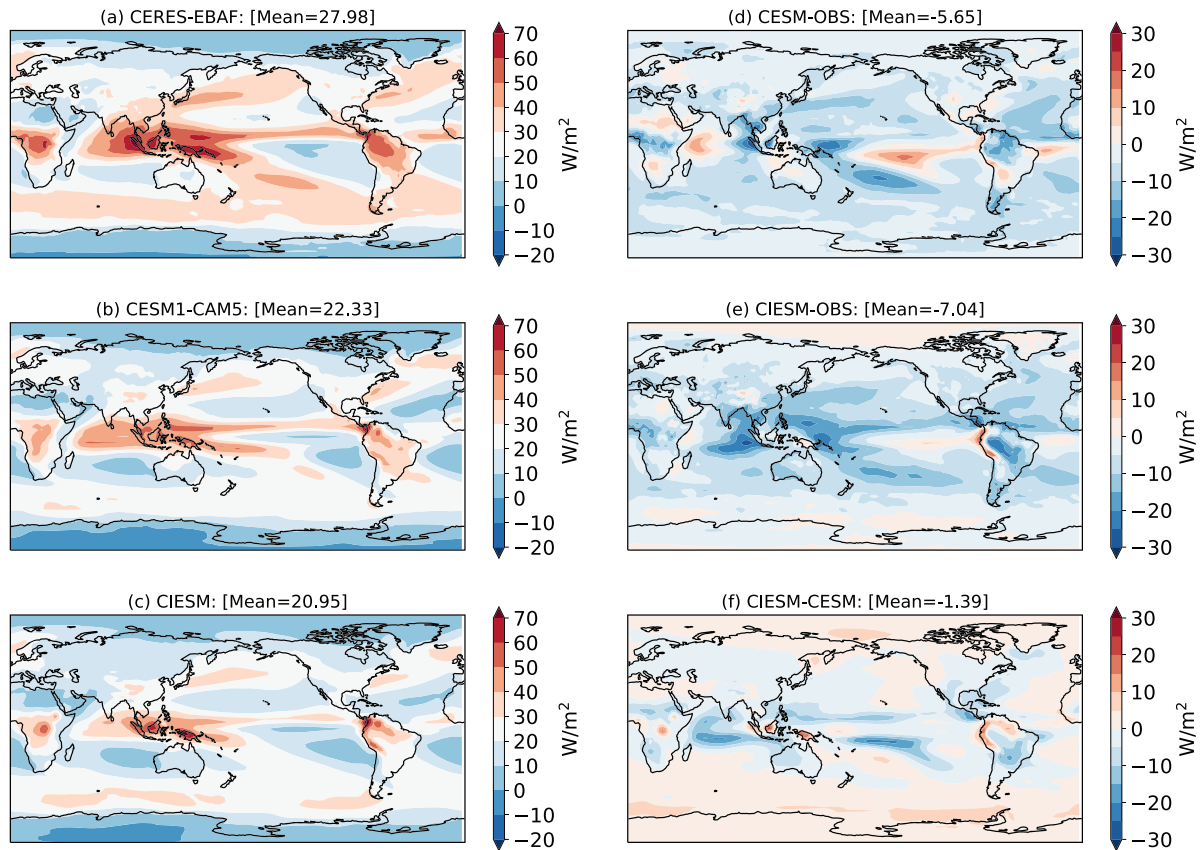
Figure 4. Same as Figure 3 but for LWCF.

(~25 Wm^{-2}, not shown), which are closely related to the underestimated sea ice coverage in CIESM (see Figures 16 and 17). Sea ice bias reduction will be one of the goals for the next round of model development. The AMIP simulation (Figure 2b) has a smaller imbalance of 0.25 Wm^{-2} and shares similar spatial distribution of biases as that of the coupled historical simulation (Figure 2c), except that biases in the Southern Ocean are slightly smaller.

The global annual mean SWCF (i.e., the difference of TOA net shortwave flux between the all-sky and clear-sky conditions; Figure 3a) from CERES-EBAF is −45.68 Wm^{-2} with large values over regions having highly reflective clouds, such as the tropical ITCZ, subtropical marine stratocumulus, and midlatitude storm tracks. For comparison, we include SWCF of CESM1 historical simulation (Figure 3b), which has negative bias over the deep tropics and positive bias over the subtropical stratocumulus regions off the west coasts of North America, South America, and Africa (Figure 3d). There are also positive biases over the Arctic and Southern Ocean in CESM1 as noted before (Kay et al., 2016). These biases are alleviated in CIESM (Figure 3e), especially over the tropical land area, southeastern subtropical Pacific, and Southern Ocean. But the bias over the northeastern subtropical Pacific is slightly amplified. This is consistent with Qin et al. (2018), who noted that the PDF cloud scheme improved marine boundary layer clouds, especially over the stratocumulus and trade wind regions, but its impact on the stratus near the coast is not as effective as that over the stratocumulus region further offshore. Another point to note is that CIESM has a much larger net flux of energy than the observation over southeastern China (Figure 3e), which is probably related to either the underestimated aerosol forcing there provided by CMIP6 or the prescribed aerosol forcing of MACv2-SP. Overall, the global average SWCF bias (−2.07 Wm^{-2}) in CIESM is slightly smaller than CESM1 (−3.1 Wm^{-2}). Similar to TOA net radiation (Figures 2 and S1), annual mean SWCF bias at high latitudes is dominated by the bias over the Arctic and Southern Ocean (south of 60°S) in JJA and DJF, respectively (Figure S2). Note that SWCF bias is about half of TOA net radiation bias over these two regions. This indicates that the contribution of underestimated sea ice coverage to TOA net radiation bias is comparable to SWCF.
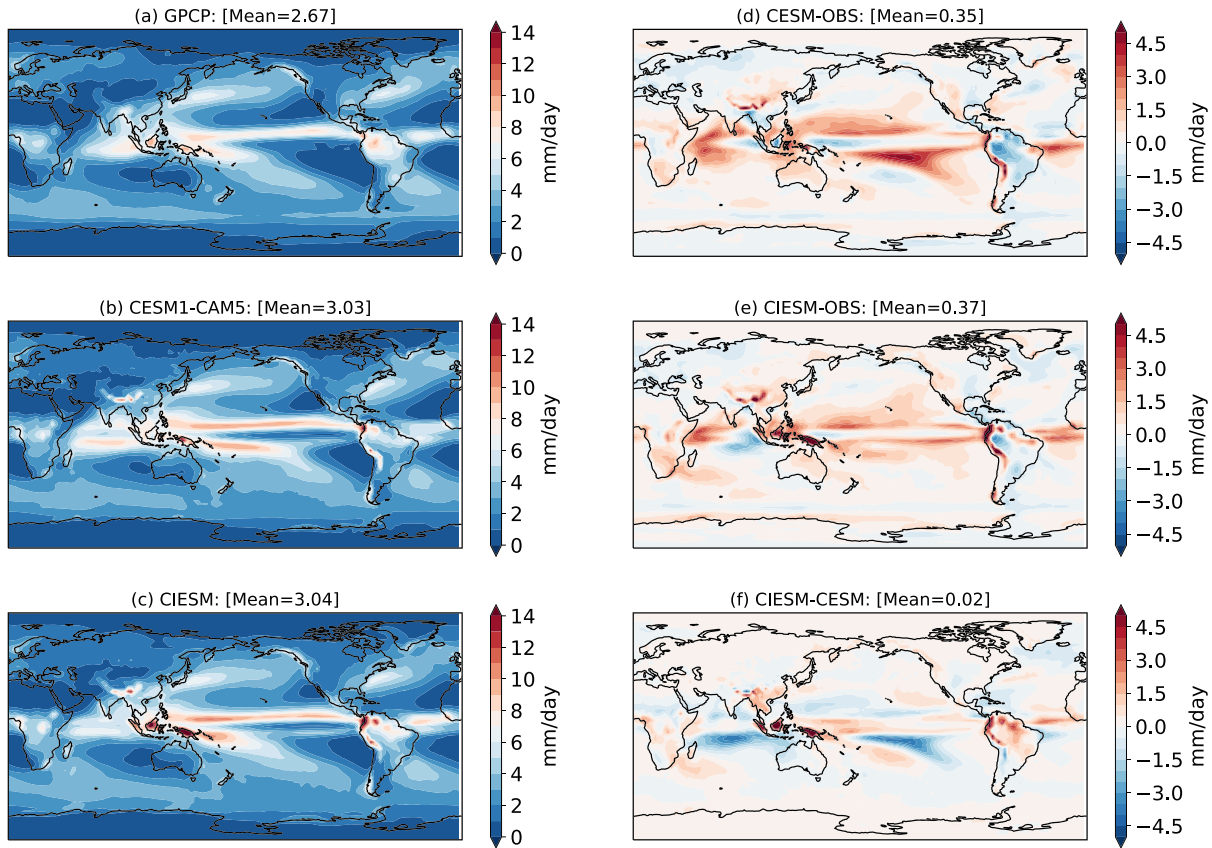
Figure 5. Annual mean precipitation distribution of (a) GPCP, (b) CESM1, and (c) CIESM. (d) Bias of CESM1 relative to GPCP and (e) bias of CIESM relative to GPCP. (f) Precipitation difference between CIESM and CESM1. Global mean value is also shown for each panel.
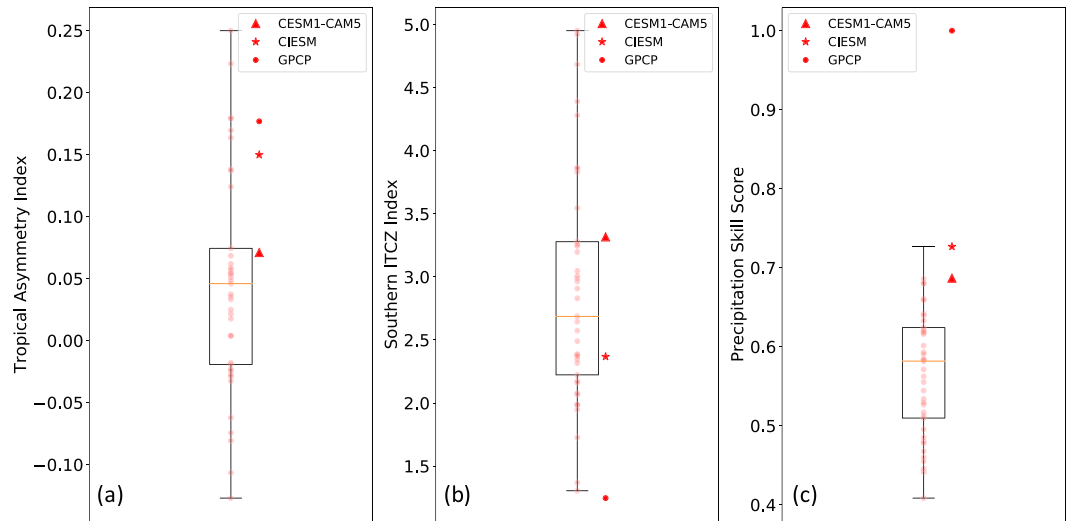

Figure 6. Comparison of tropical precipitation performance of CIESM with CESM1 and 40 CMIP5 models. (a) The asymmetry index (precipitation difference between the northern [0–20°N] and southern tropics [0–20°S] normalized by the tropical mean [20°S to 20°N]), (b) the southern ITCZ index defined as the mean precipitation over southeastern Pacific Ocean (0–20°S, 100–150°W), and (c) the precipitation skill score over the tropics (20°S to 20°N, 0–360°; see Equation 4 in Qin & Lin, 2018, for details). Box and whiskers show the first and third quartiles, minimum and maximum of 40 CMIP5 models. CMIP5 models are presented by light red dots.
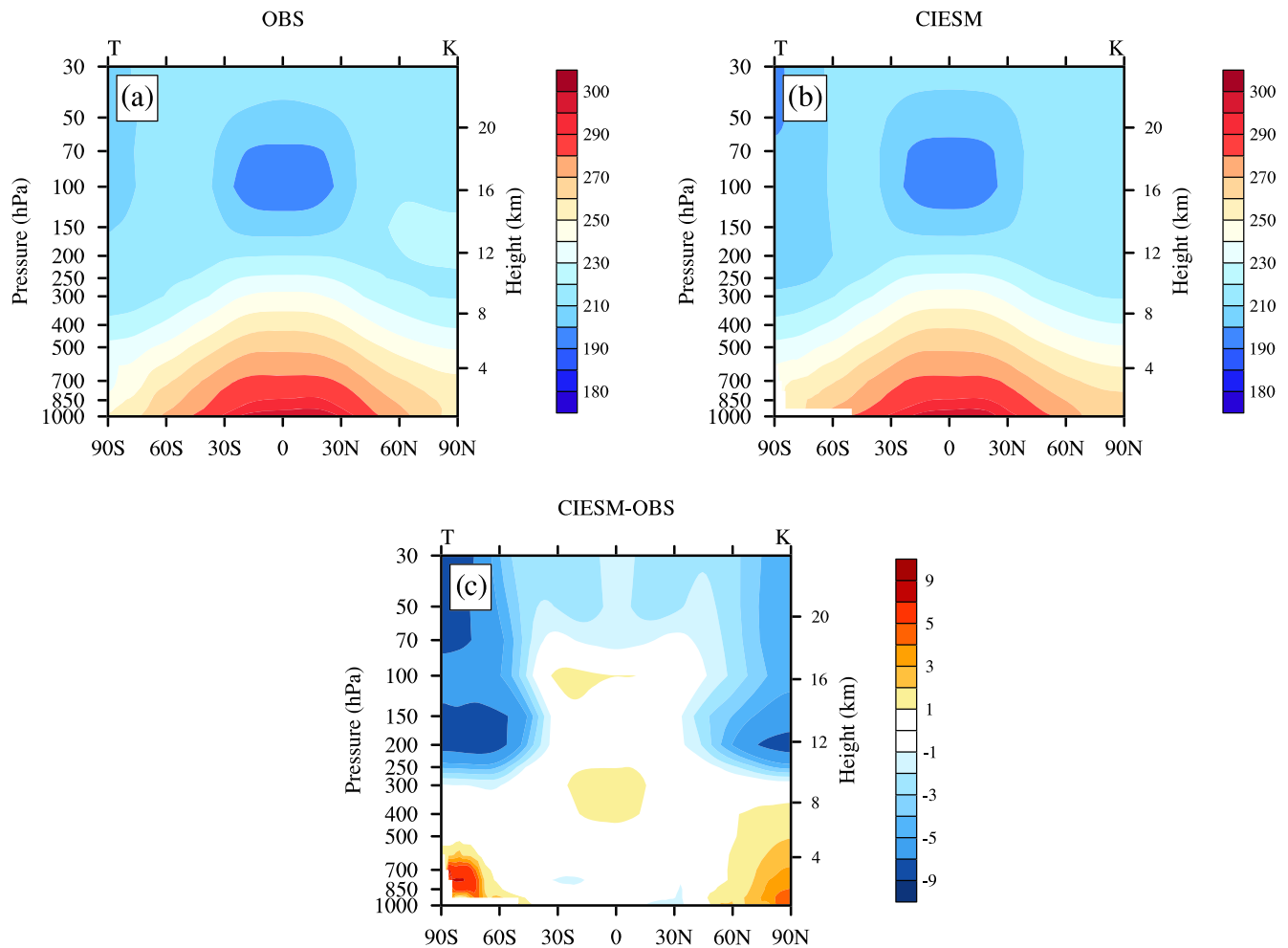
Figure 7. Annual zonally averaged temperature (K) of (a) ERA-Interim reanalysis, (b) ensemble mean of historical coupled simulations (1985–2014), and (c) model bias. Vertical coordinate is pressure level (hPa).

On the other hand, longwave cloud forcing (LWCF) is mainly regulated by high clouds, which are dominated by deep convection over the tropics (Figure 4a). Both CESM1 and CIESM have negative LWCF biases almost over the whole tropics with large biases over the convective zones except for a tongue extending from equatorial east Pacific to the middle Pacific (Figures 4d and 4e). In general, CIESM has similar spatial distribution of LWCF biases in the tropics as CESM1 but with slightly larger values. This gives a LWCF bias of -7.04 Wm^{-2} for CIESM and -5.65 Wm^{-2} for CESM1 compared to the global average of CERES-EBAF (27.98 Wm^{-2}). Note that CIESM has larger LWCF over the Arctic and Southern Ocean than CESM1. Figure S2 indicates that these positive LWCF biases are dominant over the Arctic and Southern Ocean in DJF and JJA, respectively.

Figure 5 shows the annual mean precipitation compared to Global Precipitation Climatology Project (GPCP) v2.2 (Adler et al., 2003; Huffman et al., 2009). Global mean precipitation is 3.03 and 3.04 mm day^{-1} for CESM1 and CIESM (Figure 5c), respectively. Although these values are slightly larger than GPCP estimate (2.67 mm day^{-1}), it lies within the uncertainty range as suggested in recent studies (Stephens et al., 2012; Wild et al., 2013) and CMIP5 models. CESM1 has positive biases straddling the equator over the tropical Pacific Ocean with too much precipitation extending to the middle-eastern tropical Pacific Ocean. There are also positive bias toward Western Indian Ocean and dry bias over the Amazon (Figure 5d). In comparison, these biases are reduced in CIESM (Figure 5e). For example, the prominent dry bias along the equator and wet bias extending to the mid-eastern tropical Pacific Ocean are alleviated, although rainfall is still too much south of the equator toward eastern tropical Pacific Ocean (Figure 5e). As discussed in Qin and
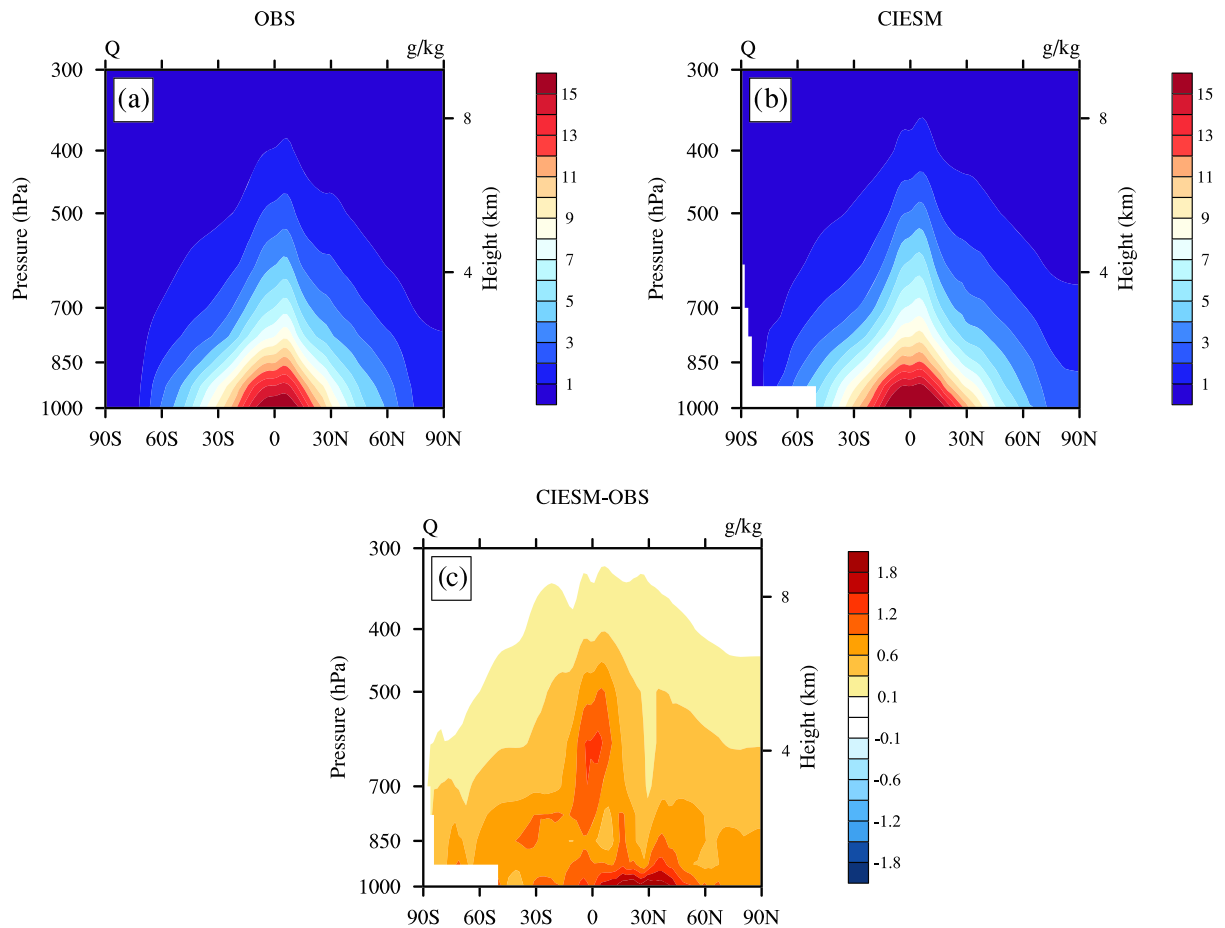
Figure 8. Same as Figure 7 but showing annual zonally averaged specific humidity (g kg^{-1}).

Lin (2018), this alleviation is mainly related to the use of the new PDF cloud scheme, which influences the radiation and SST bias and resultant Walker circulation change. Dry Amazon bias is also alleviated in CIESM compared to CESM1. CIESM has much larger precipitation over the big islands in the Maritime Continent than CESM1 (Figure 5f). Nevertheless, some biases persist, such as the dry central United States and wet northwestern Indian Ocean. These biases are more outstanding in JJA and DJF (Figure S3). For example, rainfall over the Indian subcontinent is underestimated, and there is a pronounced overestimation of rainfall south of the equator in the western Pacific in JJA (Figure S3c). In DJF, there is an overestimated rain belt protruding from western Indian Ocean all the way to the tropical Pacific Ocean north of the equator with dry bias south of the equator (Figure S3).

For a better quantification of the tropical precipitation and double ITCZ problem, the tropical precipitation asymmetry index, southern ITCZ index, and precipitation skill score from CESM1, CIESM, and 41 CMIP5 models (Table S1) are calculated as in Qin and Lin (2018) (Figure 6, see figure caption for definition of these indices). CIESM compares favorably with CMIP5 models and better than CEMS1 in terms of all the three measures (Figure 6). For example, the asymmetry index of CIESM is 0.15, better than the median of CMIP5 models (0.05) and CESM1 (0.07), much closer to 0.20 of the GPCP (Figure 6a). The skill score of CIESM also increases from that of CESM1 and becomes better than most CMIP5 models (Figure 6c). This suggested that CIESM has an overall improvement of tropical precipitation than CESM1, which was already one of the better models compared to CMIP5 models.

The annual, zonally averaged temperature and specific humidity for the coupled simulations are compared to ERA-Interim reanalysis (Dee et al., 2011) in Figures 7 and 8. Overall, the model captures the thermal structure of the atmosphere well with warm biases in the lower troposphere at higher latitudes and the
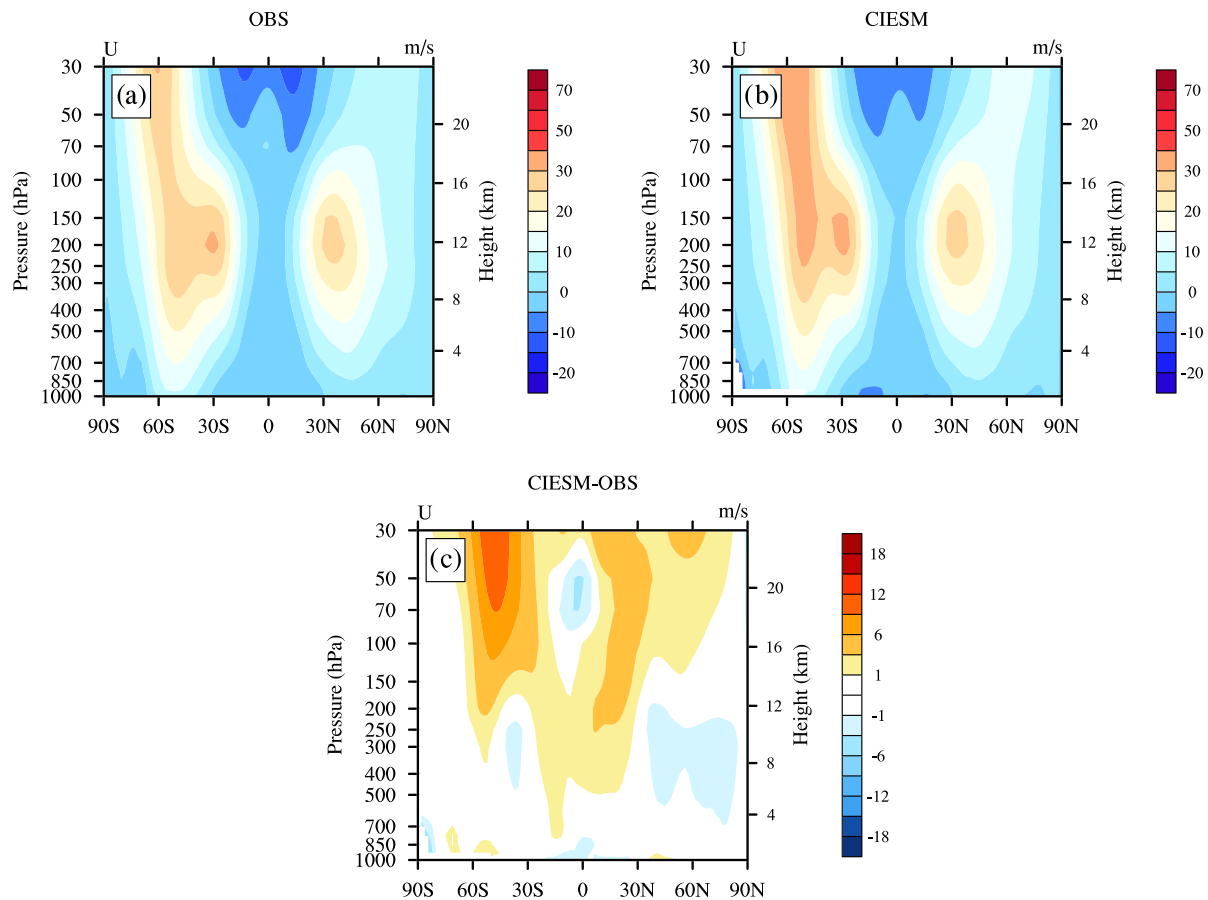
Figure 9. Same as Figure 7 but showing annual zonally averaged zonal wind (m s^{-1}).

tropical upper troposphere (300–400 hPa). There are cold biases in the lower stratosphere at higher latitudes. The model has an overall wet bias in the whole troposphere probably related to the tuning of the rain evaporation efficiency in the ZM scheme (Figure 8). The wet bias is most prominent near the surface in the northern tropics and subtropics. There is also a wet bias in the middle troposphere over the equator (Figure 8c).

Annual zonally averaged zonal winds are compared to ERA-Interim reanalysis in Figure 9. Both the midlatitude and subtropical jet are well captured (Figures 9a and 9b). Consistent with the thermal bias, the model overestimates the midlatitude jet, especially toward the lower stratosphere near 50°S related to the larger meridional temperature gradient there (Figure 7). Easterlies in the tropical upper troposphere (50–70 hPa) is slightly underestimated.

Seasonal mean large-scale climate of CIESM is compared to CMIP5 models and CESM1 using the PCMDI Metrics Package (Figure 10; Gleckler et al., 2016). The same CMIP5 data are used as that in Golaz et al. (2019). Overall, both CESM1 and CIESM have better performance for most variables compared to most CMIP5 models. Except for 500-hPa geopotential height, most variables are slightly improved or comparable between CIESM and CESM1. Shortwave cloud radiative effect (rstcre) and net longwave flux (rlut) at TOA are better in CIESM than CESM1. Notably, CIESM has a favorable surface stress (tauu and tauv) performance among all the models with good performance of precipitation in all four seasons (Figure 10).

4.2. Land Climatology

Since soil organic matter can influence the filtration of soil moisture and moisture flux, we compared the long-term-averaged (1985–2014) soil moisture simulated with the European Space Agency Climate Change Initiative (CCI) data (Dorigo et al., 2017) in Figure 11. We used the average of the first three layers of CLM4.0 for comparison since the depth is 6.22 cm, close to the penetration depth of the most microwave
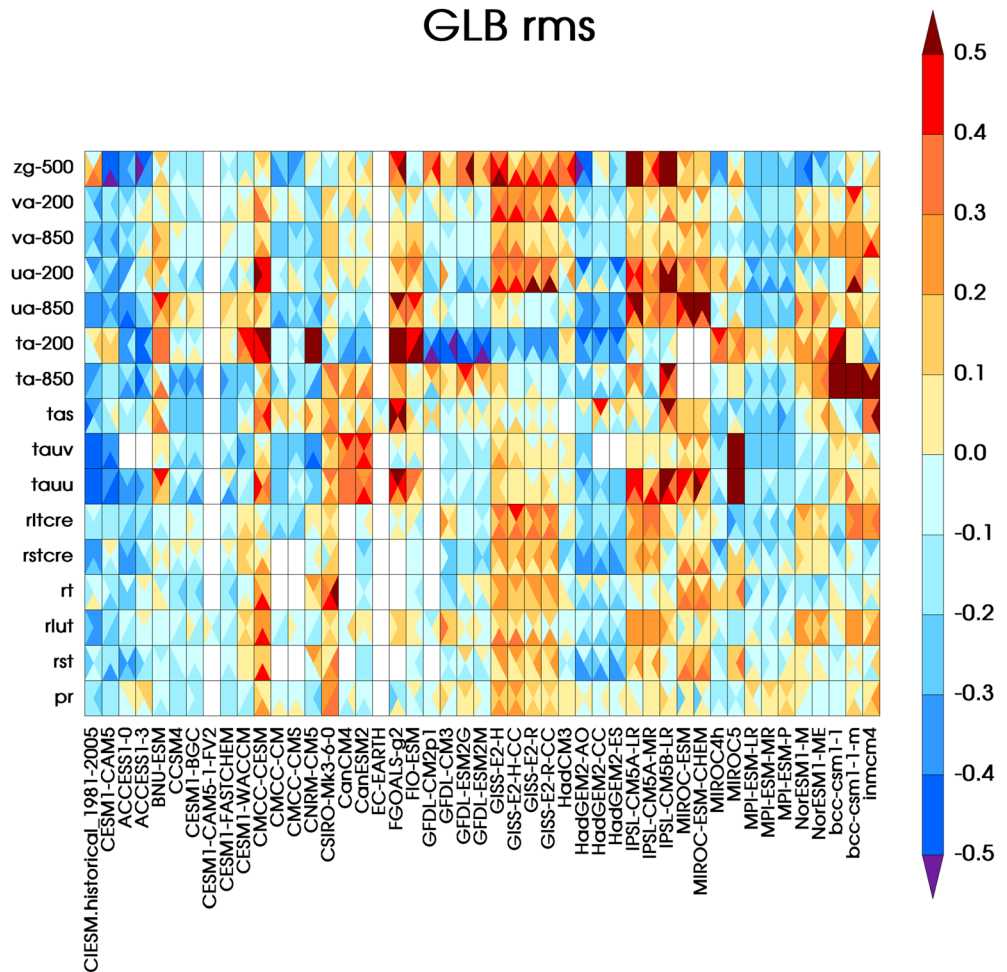
Figure 10. Comparison of CIESM historical simulation with NCAR CESM1 and CMIP5 models using the PCMDI metrics package Version 1.1.1 portrait plot (Gleckler et al., 2016). The color scale depicts a model's RMSE as a relative error (unitless) normalized by the median error of all CMIP5 model results shown in the figure. For example, a value of −0.20 indicates that a model's RMSE is 20% smaller than the median error for that variable across all simulations on the figure. The triangles in each grid square show results for four individual seasons (from left rotating clockwise are for JJA, SON, DJF, and MAM seasons) from multiple global fields (zg-500 = 500-hPa geopotential height; va-200 and va-850 = 200- and 850-hPa meridional wind; ua-200 and ua-850 = 200- and 850-hPa zonal wind; ta-200 and ta-850 = 200- and 850-hPa air temperature; tas = surface air temperature; tauv and tauu = meridional and zonal wind stress over ocean; rltcre and rstcre = longwave and shortwave cloud radiative effect at TOA; rt = net radiative flux at TOA; rlut and rst = net longwave and shortwave flux at TOA; pr = precipitation).

frequencies used to generate European Space Agency CCI soil moisture product. It is clear that CIESM simulated dry soil moisture in arid and semiarid zones, with the driest centers located in the Sahel desert. Similar to CCI, the wet belt in Euro-Asian continent from 45°N to 60°N was well captured by CIESM. The difference map shows that CIESM soil moisture is slightly larger than CCI with biases mostly falling within a range of [−0.1 to 0.1]. Given the facts of huge heterogeneity in the top layers of land surface as well as the uncertainty in the remote sensing products, CIESM gives a reasonable estimate of land surface soil moisture status.

4.3. Ocean Climatology

Compared to the Hadley-National Oceanic and Atmospheric Administration/OI merged data product (Hurrell et al., 2008) averaged over 1985–2014 period, CIESM captures the spatial pattern of SST well especially over the tropics, with biases generally less than 1°C except off the west coasts of North America, South America, and Africa (Figure 12c). The warm bias is mainly over the Southern Ocean, especially toward the
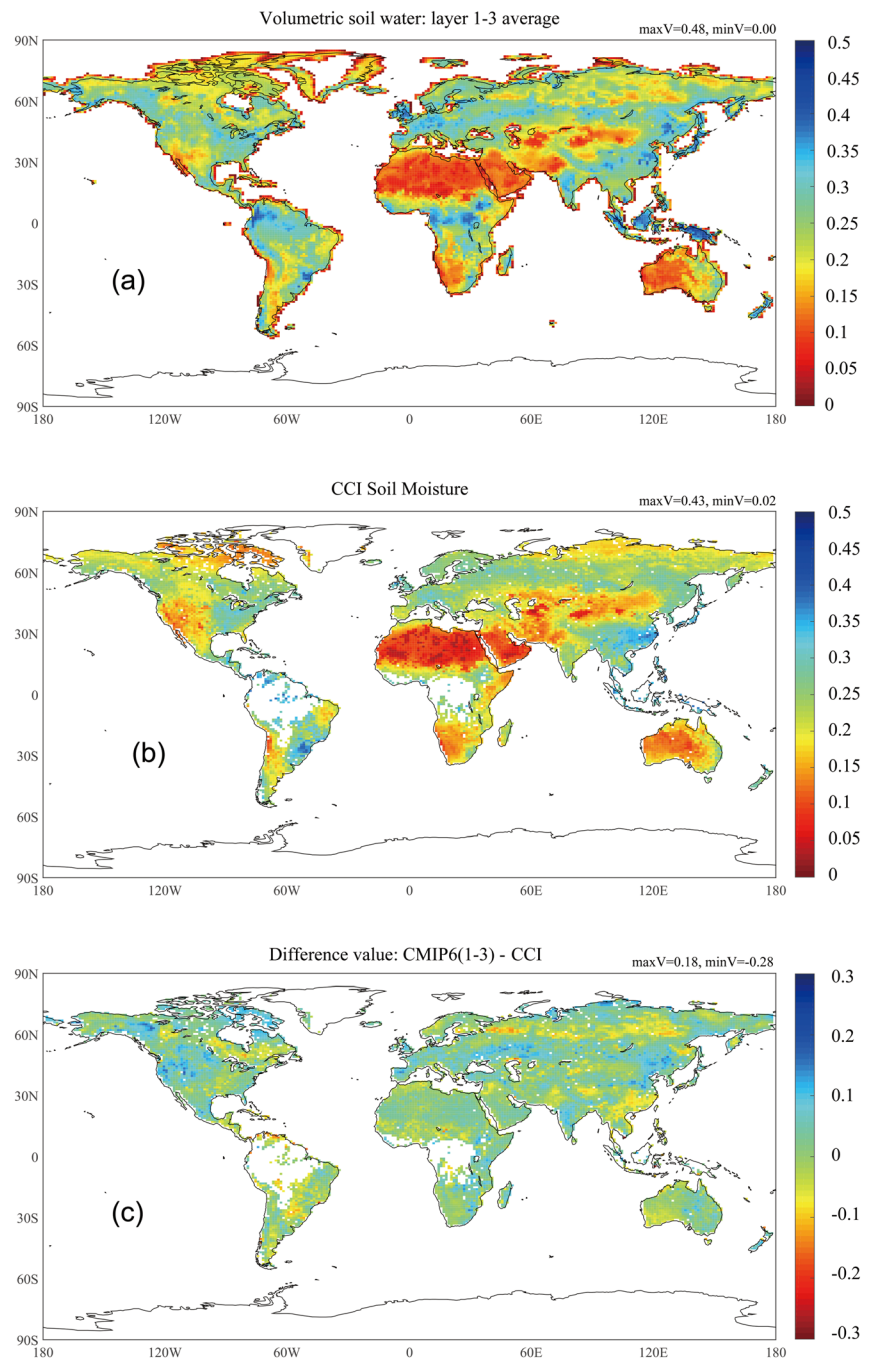
Figure 11. Volumetric soil moisture from (a) CIESM simulation, (b) ESA CCI, and (c) their differences.

Indian Ocean sector (Figure 12c). There is also warm bias extending from the west coast of America and Africa, probably related to the stratus-related shortwave bias as mentioned in section 4.1. Warm bias up to 2°C exists over the Gulf of Alaska, but there is a cold bias south of Greenland in the north Atlantic Ocean. The global mean bias is 0.66°C with a RMSE of 1.17°C. Warm biases over the high latitudes are larger in warm seasons. For example, warm bias over the Southern Ocean is larger in DJF, and bias over the Arctic and Gulf of Alaska is more prominent in JJA (Figure S4). This is mainly related to the warmer piControl states (Figure 1) and stronger warming in the historical simulations as discussed below.

Sea surface salinity (SSS) has large values over the subtropical oceans, especially in the Atlantic Ocean in both observations (Figure 13a) and model simulations (Figure 13b). CIESM is able to capture the overall
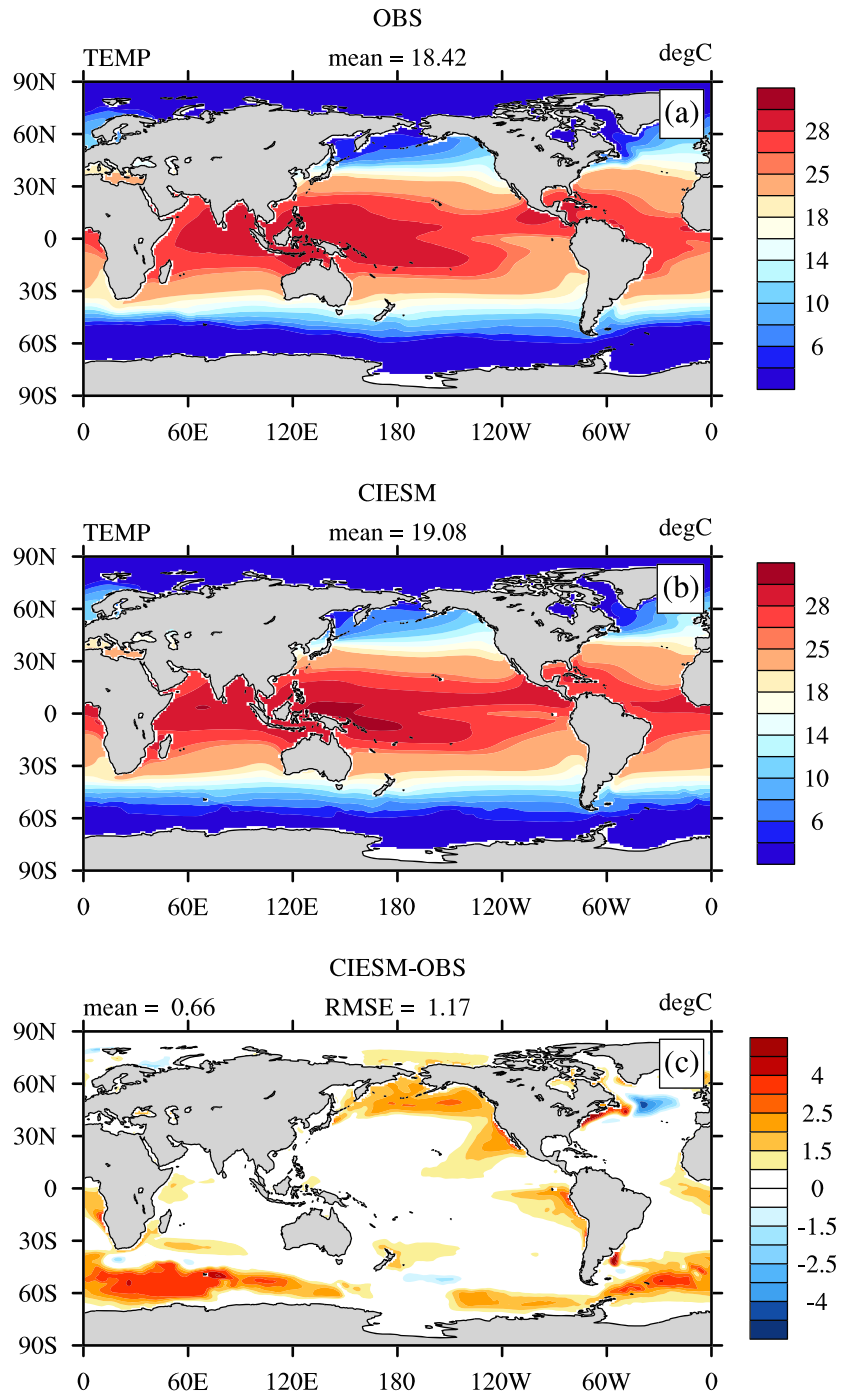
Figure 12. Annually averaged sea surface temperature climatology (1985–2014) for (a) Hadley-National Oceanic and Atmospheric Administration/OI merged sea surface temperature data set (1985–2014; Hurrell et al., 2008), (b) CIESM historical simulation (ensemble mean), and (c) model bias.

spatial distribution of SSS with salty bias in the southeast Pacific Ocean and northern subtropical Atlantic Ocean (Figure 13c). Similar to most CMIP5 models, there is a fresh bias in the northern Atlantic Ocean south of Greenland. There is also fresh bias in the eastern sector of the Arctic Ocean probably related to the underestimated sea ice there. The seasonal variability of SSS bias is rather small with slightly enhanced fresh bias surrounding the Antarctic in DJF (Figure S5) probably related to the much less sea ice there.
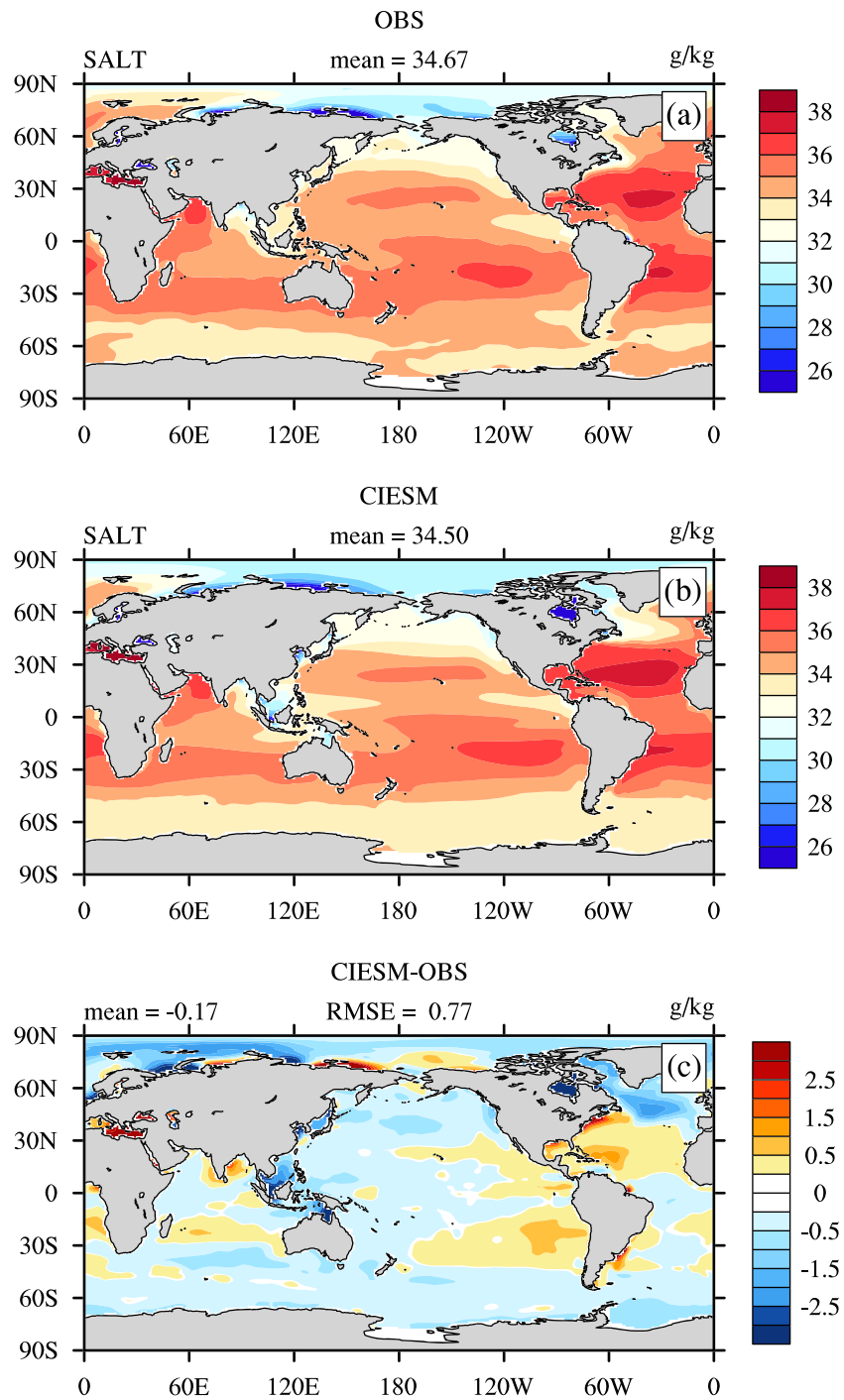
Figure 13. As in Figure 12 but for sea surface salinity (PSU). The data set in (a) is from Polar Science Center Hydrographic Climatology Version 2 (Steele et al., 2001), (b) CIESM historical simulation (ensemble mean), and (c) model bias.

The AMOC is a climatically important ocean circulation. The 1850–2014 average Eulerian-mean AMOC of one historical simulation is shown in Figure 14. The maximum overturning is up to 21 Sv occurring near 35°N at a depth near 1 km. At the site of the RAPID array near 26°N, the model produces a transport of ~15 Sv, slightly smaller than the observed value of 16.9 Sv (Smeed et al., 2016). Below 3 km, there is some indication of the northward flowing Antarctic Bottom Water with transport less than 1 Sv. Figure 15 shows the time evolution of maximum AMOC at 26°N from the three historical simulations. Simulated AMOC
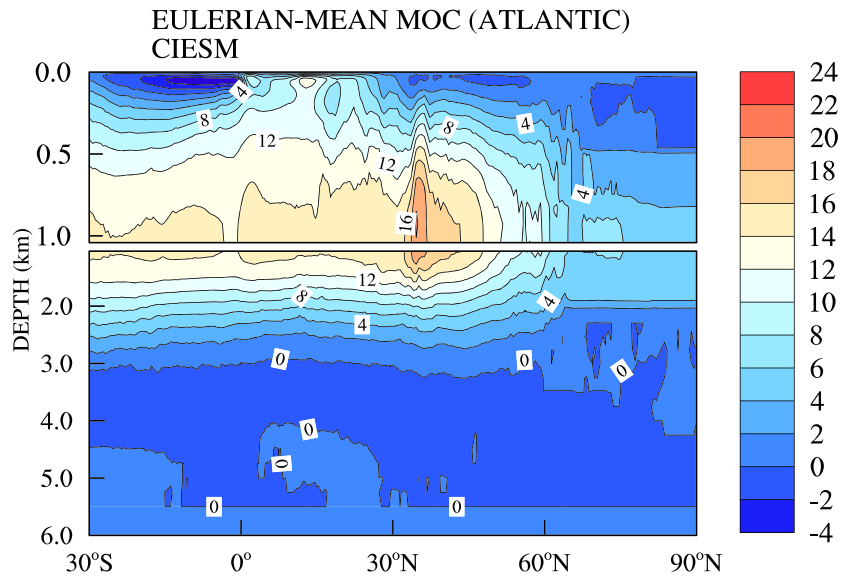
Figure 14. The 1850–2014 average Eulerian-mean Atlantic meridional overturning circulation (in Sv) from one of the historical simulations.

strength is close to the observation, but it has a downward trend after ~1960s in all the three simulations. Whether such a reduction is related to the larger warming trend of the simulations (Figure 19) warrants further investigation.

4.4. Sea Ice

Model- and satellite-measured (from special sensor microwave imager) mean sea ice fraction differences in the Arctic and Antarctic are shown for March and September in Figure 16. In March, CIESM
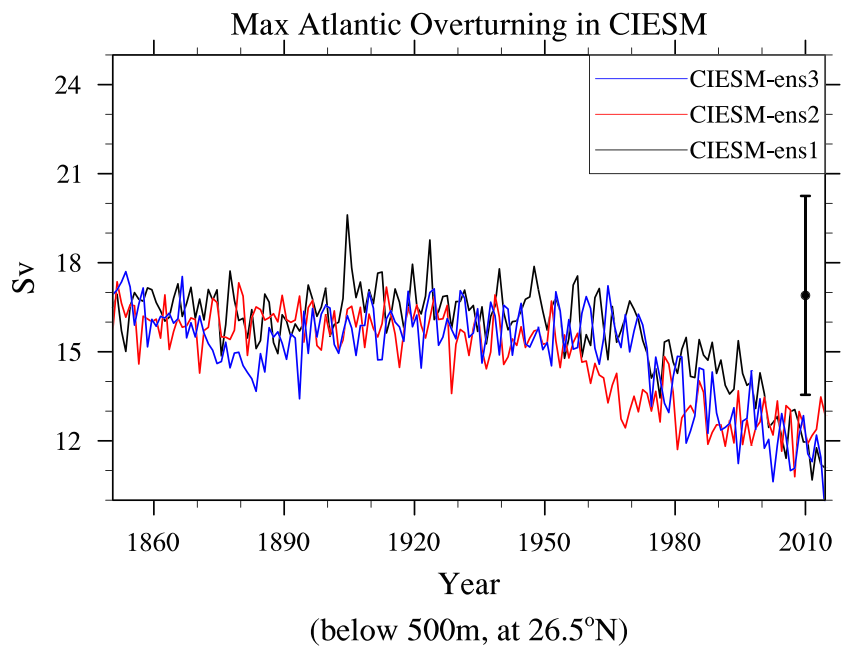

Figure 15. Annually averaged maximum Atlantic Meridional Overturning Circulation at 26.5°N below 500-m depth. The three lines indicate the three historical simulations. The observed Atlantic Meridional Overturning Circulation and standard deviation at the RAPID array are shown by the black vertical bar (16.9 ± 3.35 Sv).
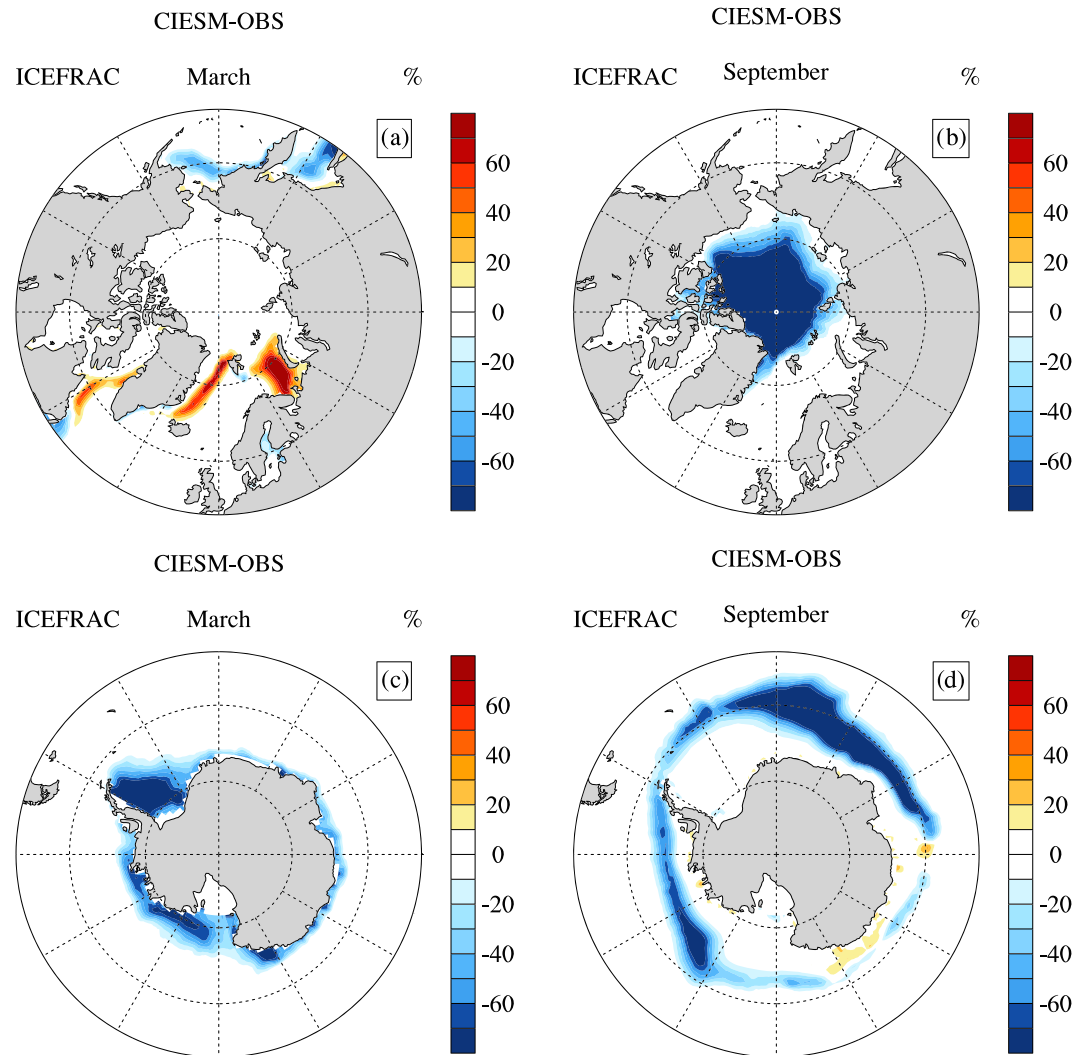
Figure 16. CIESM-simulated sea ice fraction biases relative to NSIDC measurements (1985–2014) in March and September in Arctic Ocean (a, b) and Circum-Antarctic Ocean (c, d).

produces a good simulation of sea ice fraction in the Arctic except not as extensive as observed in the Pacific sector and too much in the North Atlantic section. However, sea ice fraction is significantly underestimated in September in the Arctic (Figure 16b). It means that the Arctic is too warm during the boreal summer (see Figure 7c too), coincident with the strong positive shortwave bias discussed above.

In the Antarctic, model tends to underestimate sea ice fraction almost everywhere in both March and September. This is consistent with the SST warm bias over the Southern Ocean noted above. The reason for the warm bias is complicated, partly related to the underestimated marine boundary layer clouds in the Southern Ocean and ocean mixing there. Model seasonal variation of sea ice extent (SIE) is compared with National Snow and Ice Data Center observations in Figure 17. Observed Arctic SIE was up to 16×10^6 km^2 and decreased to 6×10^6 km^2 in September. The model produced larger SIE than observed in winter and spring but significantly underestimated SIE in fall (Figure 17a). In the Antarctic, the model captured the seasonal variation of SIE well with an overall underestimation of 3–4×10^6 km^2 (Figure 17b). September Arctic SIE in the initial time of the three historical integration is already very low (~1×10^6 km^2, not shown). A close investigation of underestimated sea ice in the warm season is warranted in the future.
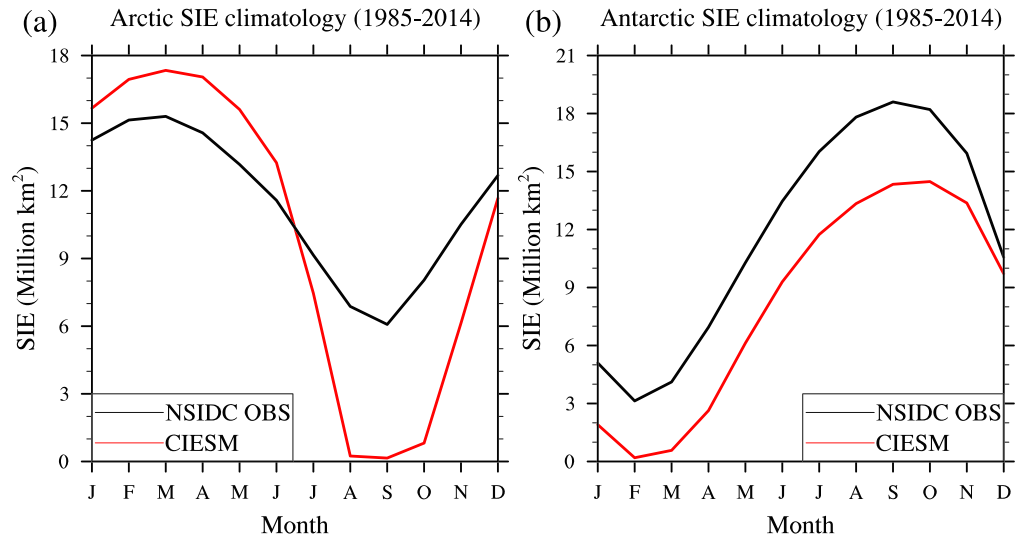
Figure 17. Seasonal evolution of sea ice extent of CIESM compared with NSIDC measurements for (a) Arctic and (b) Antarctic.

4.5. ENSO Characteristics

ENSO characteristics from the piControl and historical simulations are compared with HadISST (Rayner, 2003) using a wavelet analysis of Nino 3.4 SST in Figure 18. ENSO in the observations has a broad spectrum between 3 and 7 years with a maximum power of ~10 K^2. The seasonal cycle shows maximum

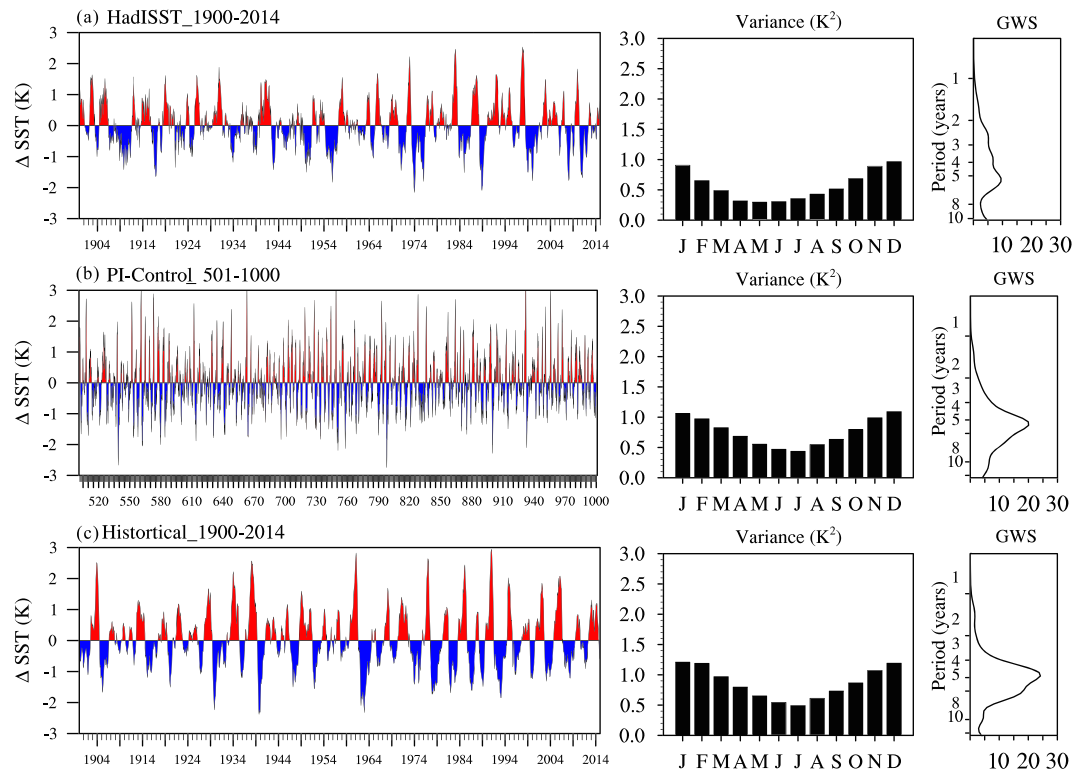**Figure 18.** (a) Time evolution of the monthly Nino-3.4 SST anomalies (K) for detrended observations (HadISST, 1900–2014) (left column), seasonal variation of time-averaged Nino-3.4 SST variance (K^2, middle column), and time-averaged wavelet power spectra of the Nino-3.4 SST index (K^2, right column). (b) Same as (a) but for the 500-year piControl simulation. (c) Same as (a) but for one historical simulation (1900–2014).
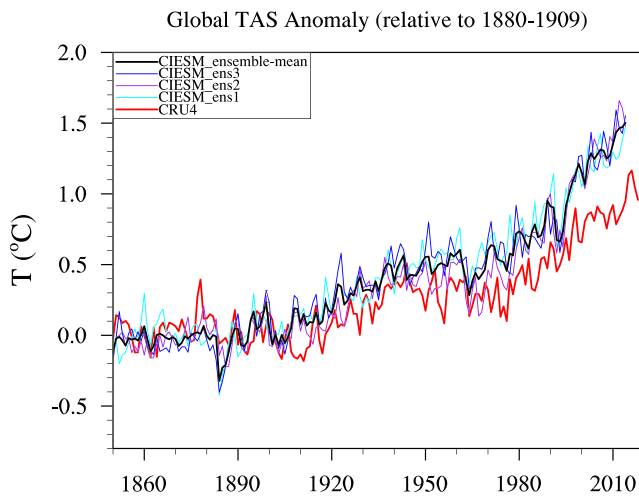
Figure 19. Time evolution of annual global mean surface air temperature anomalies (with respect to 1880–1909) between the three CIESM historical simulations and HadCRUT4 (red line). Black line is the ensemble mean.

variances ($\sim 1\ K^2$) in boreal winter and minimum near April ($\sim 0.4\ K^2$). Similarly, both piControl and historical simulations have a broad spectrum between 3 and 8 years, although the power is too large with a peak near 4–5 years. Both simulations also well capture the seasonal cycle with slightly larger magnitudes (maximum value of ~ 1.1–$1.2\ K^2$ in January). This is an improvement relative to CCSM4 (Deser et al., 2012) and CESM1.2.1 (not shown). Note that ENSO simulation has been improved in terms of both period and magnitude in the new CESM2 (Danabasoglu et al., 2020). CIESM still has a seasonal cycle that lags the observations by 2–3 months with a maximum in January and a minimum in July. The reduced magnitude of ENSO in CIESM is partly related to the new air-sea flux parameterization and the enhanced tidal mixing introduced. Ocean vertical mixing also plays a role as noted during the development stage.

4.6. Historical Warming and Climate Sensitivity

Global mean surface air temperature anomaly relative to 1880–1909 from the three ensemble historical simulations and their mean is compared with HadCRUT4 observational product (Figure 19). Although simulations well capture the observed temperature evolution before 1905, they have a positive bias of ~0.15°C than observed thereafter. The warm bias amplified gradually, especially when the simulation missed the slight cooling from 1940s to 1970s and the warming slowdown since 1998 in observations. This is not unexpected since the observed warming slowdown mainly resulted from internal climate variability, whose phase is hard to be captured by free run simulations. This is common in most CMIP5 and CMIP6 models. As a result, the ensemble mean temperature toward the end of 2014 is about 0.55°C higher than observed. This might be related to the positive TOA imbalance (Figures 1 and 2) and high climate sensitivity of the model. Note that we have not attempted to tune the historical temperature trend during the development. A close look at the NH and SH temperature evolution indicates that the much larger warming is mainly from the NH, probably related to the warm bias in the Arctic. Note that the recent warming in the Arctic might be underestimated in HadCRUT4 (e.g., J. Huang et al., 2017), and thus, the stronger warming in the model might be exaggerated as shown in Figure 19.
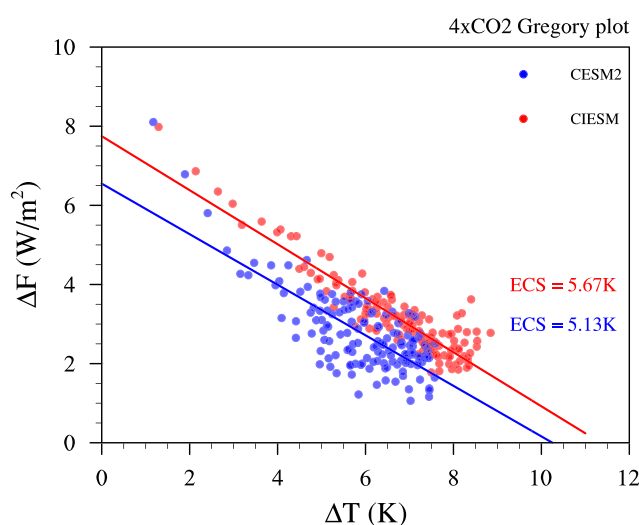

Figure 20. Global annual mean of surface air temperature changes versus TOA net radiation changes for 150 years of abrupt-4×CO$_2$ simulation relative to the piControl simulation for CESM2 (blue) and CIESM (red). Linear regression is depicted with the solid line, whose intersection with the horizontal axis is twice of the equilibrium climate sensitivity (ECS).

We use the idealized abrupt 4 times CO_2 simulation to estimate climate sensitivity following Gregory et al. (2004) as in Zelinka et al. (2020). The Equilibrium Climate Sensitivity (ECS) is estimated to be 5.67 K (Figure 20). For comparison, ECS from CESM2 is 5.13 K, which is similar to Zelinka et al. (2020) but smaller than that estimated using slab ocean simulations by Gettelman et al. (2019). Both are larger than most CMIP5 models. Note that there are more CMIP6 models having larger ECS (Bodas-Salcedo et al., 2019; Gettelman et al., 2019; Golaz et al., 2019; Voldoire et al., 2019). For example, there are already nine models in CMIP6 having ECS exceeding the CMIP5 maximum (Zelinka et al., 2020) and five models exceeding 5 K (Flynn & Mauritsen, 2020). Such an upward shift toward higher ECS has been attributed to increased positive shortwave cloud feedback, for example, over the Southern Ocean (Flynn & Mauritsen, 2020) and extratropical regions (Zelinka et al., 2020). Added or modified aerosol-cloud interactions also contribute to ECS (Gettelman et al., 2019). Increased positive shortwave cloud feedback might be partly related to the more complex cloud schemes used and more realistic clouds simulated in CMIP6 models (Gettelman et al., 2019; Tan et al., 2016; Zelinka et al., 2020). The plausibility of higher ECS needs to be investigated and evaluated using different lines of evidence.
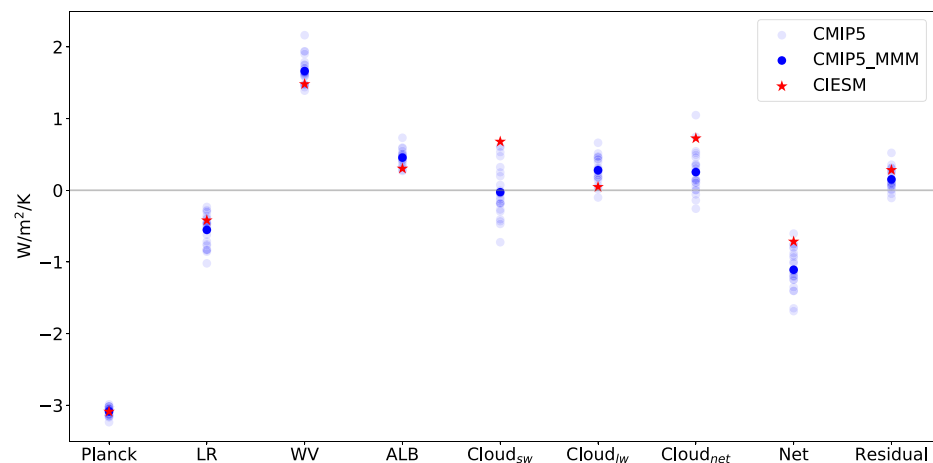
Figure 21. Estimates of global and annual mean radiative feedbacks of 25 CMIP5 models (light blue circles with the multimodel mean denoted as a blue circle) and CIESM (red star) from abrupt-4×CO_2 simulations. The net radiative feedback is broken down into Planck, lapse rate (LR), water vapor (WV), surface albedo (ALB), shortwave cloud ($Cloud_{SW}$), longwave cloud ($Cloud_{LW}$), net cloud ($Cloud_{net}$), and residual term (Residual) using radiative kernels of J. Huang et al. (2017) as Zelinka et al. (2020).

To better understand the sources of higher ECS of CIESM and compare with other CMIP5 models, we diagnosed the radiative feedback from abrupt-4×CO_2 simulation. Similar to Zelinka et al. (2020), the radiative kernel derived by J. Huang et al. (2017) was used and applied to 25 available CMIP5 models and CIESM (Figure 21). Except for cloud radiative feedback, other feedbacks (Planck, lapse rate, water vapor, and albedo) are close to the multimodel mean of CMIP5 models. The albedo feedback appears to be weaker than the multimodel mean and touches the lower bound of CMIP5 models, which is likely related to the much less sea ice fraction in CIESM. The net cloud feedback is larger than all but one CMIP5 model, and shortwave cloud feedback is the dominant factor (larger than all CMIP5 model shown in Figure 21) with smaller long-wave cloud feedback (close to zero). The net feedback of CIESM (-0.72 Wm^{-2} K^{-1}) is less negative than the CMIP5 mean (-1.11 Wm^{-2} K^{-1}) and thus corresponds to the much larger ECS. Further investigation indicates that low clouds contribute significantly to the positive shortwave cloud feedback in the subtropics and midlatitudes (not shown). CIESM tends to produce more cloud water than CESM1 due to the use of PDF cloud scheme (Qin et al., 2018). It also has more supercooled liquid water in the mixed-phase clouds with the use of single ice microphysics (Zhao et al., 2017). Both might reduce the negative optical depth cloud feedback in the Southern Ocean and extratropical regions as suggested by several studies (Bodas-Salcedo et al., 2019; Tan et al., 2016; Zelinka et al., 2020). Note that aerosol-cloud interactions are prescribed using the MACv2-SP approach in CIESM and thus would not influence ECS. More detailed exploration of the positive cloud feedback will be reported later.

5. Summary and Discussion

A team effort of model development, including various model modifications and developments, toward the first version of CIESM is introduced. Modifications in the atmospheric model include a modified deep convection scheme, a diagnostic statistical cloud macrophysics scheme, a single ice microphysics scheme, a four-stream shortwave radiation scheme, and an orographic form drag parameterization. In the ocean component, a more efficient parallel barotropic solver was introduced with modified tidal mixing. An air-sea flux scheme to enhance the wind stress over regions with large SST gradients is used to improve transient variabilities over the tropical and western boundary current regions. In the land model, new soil property data are used with a new thermal roughness parameterization. Finally, a new coupler, C-Coupler2, is employed to handle coupling among the component models and to improve the flexibility of the coupling architecture of CIESM.

The model was ported to the supercomputer Sunway TaihuLight developed in China, and all the CMIP6 DECK simulations were conducted on it. A high-resolution version of the CIESM with a quarter-degree

atmosphere and 0.1° ocean is currently tested on this machine. Preliminary test with a quarter-degree atmosphere model has been finished and will participate in the high-resolution model intercomparison. CIESM also participated in six MIPs organized by CMIP6. The data sets from these MIPs and DECK simulations will be available on the ESGF site.

Results from a 500-year preindustrial and three historical simulations are compared with available observations. Overall, the model gives reasonable mean climate states, including SST, air temperature, specific humidity, and wind patterns. Some persistent systematic biases, such as underestimated marine boundary layer clouds and double ITCZ problem, are alleviated in CIESM. Characteristics of CIESM-simulated ENSO features, including the period and magnitude, are also improved and comparable to observations. On the other hand, some biases remain, such as the large shortwave bias over the Arctic and Southern Ocean south of 60°S, partly resulted from the significantly underestimated sea ice in warm seasons. There is also a stronger warming than observed in the historical simulations. CIESM presents a much higher climate sensitivity with an ECS up to 5.67°C, mainly associated with increased shortwave cloud feedback.

CIESM was developed based on CESM1, a state-of-the-art community model. In this sense, we are on the shoulder of a giant. As a newcomer to the modeling world, we have benefited significantly from the accumulated expertise of the community and learned a lot during this process. We hope we could contribute to the community too. For example, a collaborative analysis framework for distributed gridded environmental data to facilitate the processing and analyses of large volumes of data remotely has been developed and provided to the community (H. Xu et al., 2019). Some other ongoing development work briefly introduced here will be provided to the community. Due to the time line of the CMIP6 activities, these developments have not been included in the integrations for CMIP6 but will be gradually merged into later versions of the CIESM.

A global orthogonal model grid was constructed for POP2 using Schwarz-Christoffel conformal mappings (S. Xu et al., 2015). The grid is composed of a polar cap with an irregular turning latitude (47°N on the North Atlantic Ocean and 66°N for the Bering Strait), which uses a polar coordinate and forms an overall global dipolar grid. Other part of the grid (i.e., southern to the polar cap) is fully latitudinal and longitudinal, covering 96% of the global oceanic area. The nominal resolution of the grid is 0.5°, with the meridional refinement (0.25°) for the tropical regions (within 10° of the equator). The size of the half-degree grid is 720 and 560 in the zonal and meridional direction, respectively. With this new grid, a series of test with ocean physical parameterization schemes tailored to the new grid have been conducted.

Land ecosystems absorb approximately 30% of the anthropogenic carbon dioxide emissions. It is urgent to improve land carbon models in order to accurately predict future changes in ecosystem services and feedback to climate change. Land models traditionally represent the carbon cycle by a series of carbon balance equations to track their influxes into and effluxes out of individual pools. This representation makes it difficult to track model behaviors and computationally costly for spin-up and sensitivity analysis. We have developed a matrix approach that the carbon balance equations in original ESMs are reorganized into a matrix form without changing any modeled carbon processes and mechanisms (Luo et al., 2001, 2003, 2016, 2017; Luo & Weng, 2011; Sierra & Müller, 2015). We have developed matrix equations for NCAR's Community Land Model (Y. Huang, Zhu, et al., 2018; Rafique et al., 2017) and other global land carbon cycle models (Huang, Lu, et al., 2018; Xia et al., 2013). The matrix approach based on CLM4.5 matrix version (Y. Huang, Zhu, et al., 2018) will be used in the next version of CIESM.

Data Availability Statement

Current CIESM version is freely available online (http://doi.org/10.5281/zenodo.3596317). The data sets used in this study are freely available from the Earth System Grid Federation (ESGF) (esgf-node.llnl.gov/search/cmip6).

References

Adler, R. F., Huffman, G. J., Chang, A., Ferraro, R., Xie, P. P., Janowiak, J., et al. (2003). The version-2 Global Precipitation Climatology Project (GPCP) monthly precipitation analysis (1979-present). *Journal of Hydrometeorology*, *4*(6), 1147–1167. https://doi.org/10.1175/1525-7541(2003)004<1147:TVGPCP>2.0.CO;2

Beljaars, A. C. M., Brown, A. R., & Wood, N. (2004). A new parametrization of turbulent orographic form drag. *Quarterly Journal of the Royal Meteorological Society*, *130*(599), 1327–1347. https://doi.org/10.1256/qj.03.73

Bodas-Salcedo, A., Mulcahy, J. P., Andrews, T., Williams, K. D., Ringer, M. A., Field, P. R., & Elsaesser, G. S. (2019). Strong dependence of atmospheric feedbacks on mixed-phase microphysics and aerosol-cloud interactions in HadGEM3. *Journal of Advances in Modeling Earth Systems*, *11*(6), 1735–1758. https://doi.org/10.1029/2019MS001688

Bretherton, C. S., & Park, S. (2009). A new moist turbulence parameterization in the community atmosphere model. *Journal of Climate*, *22*(12), 3422–3448. https://doi.org/10.1175/2008JCLI2556.1

Brierley, C. M., & Fedorov, A. V. (2011). Tidal mixing around Indonesia and the Maritime continent: Implications for paleoclimate simulations. *Geophysical Research Letters*, *38*(24). https://doi.org/10.1029/2011GL050027

Cao, J., Wang, B., Yang, Y.-M., Ma, L., Li, J., Sun, B., et al. (2018). The NUIST Earth System Model (NESM) Version 3: Description and preliminary evaluation. *Geoscientific Model Development*, *11*(7), 2975–2993. https://doi.org/10.5194/gmd-11-2975-2018

Chelton, D. B., & Xie, S.-P. (2010). Coupled ocean-atmosphere interaction at oceanic mesoscales. *Oceanography*, *23*(4), 52–69. https://doi.org/10.5670/oceanog.2010.05

Chelton, D. B., Schlax, M. G., Freilich, M. H., & Milliff, R. F. (2004). Satellite measurements reveal persistent small-scale features in ocean winds. *Science*, *303*(5660), 978–983. https://doi.org/10.1126/science.1091901

Chen, Y., Yang, K., He, J., Qin, J., Shi, J., Du, J., & He, Q. (2011). Improving land surface temperature modeling for dry land of China. *Journal of Geophysical Research*, *116*, D20104. https://doi.org/10.1029/2011JD015921

Craig, A. P., Vertenstein, M., & Jacob, R. (2012). A new flexible coupler for earth system modeling developed for CCSM4 and CESM1. *International Journal of High Performance Computing Applications*, *26*(1), 31–42. https://doi.org/10.1177/1094342011428141

Danabasoglu, G., Lamarque, J. F., Bacmeister, J., Bailey, D. A., DuVivier, A. K., Edwards, J., et al. (2020). The Community Earth System Model Version 2 (CESM2). *Journal of Advances in Modeling Earth Systems*, *12*(2). https://doi.org/10.1029/2019MS001916

Danabasoglu, G., Bates, S. C., Briegleb, B. P., Jayne, S. R., Jochum, M., Large, W. G., et al. (2012). The CCSM4 ocean component. *Journal of Climate*, *25*(5), 1361–1389. https://doi.org/10.1175/JCLI-D-11-00091.1

Dee, D. P., Uppala, S. M., Simmons, A. J., Berrisford, P., Poli, P., Kobayashi, S., et al. (2011). The ERA-Interim reanalysis: Configuration and performance of the data assimilation system. *Quarterly Journal of the Royal Meteorological Society*, *137*(656), 553–597. https://doi.org/10.1002/qj.828

Deser, C., Knutti, R., Solomon, S., & Phillips, A. S. (2012). Communication of the role of natural variability in future North American climate. *Nature Climate Change*, *2*(11), 775–779. https://doi.org/10.1038/nclimate1562

Deser, C., Phillips, A. S., Tomas, R. A., Okumura, Y. M., Alexander, M. A., Capotondi, A., et al. (2012). ENSO and Pacific decadal variability in the Community Climate System Model Version 4. *Journal of Climate*, *25*(8), 2622–2651. https://doi.org/10.1175/JCLI-D-11-00301.1

Dorigo, W., Wagner, W., Albergel, C., Albrecht, F., Balsamo, G., Brocca, L., et al. (2017). ESA CCI soil moisture for improved Earth system understanding: State-of-the art and future directions. *Remote Sensing of Environment*, *203*, 185–215. https://doi.org/10.1016/j.rse.2017.07.001

Eyring, V., Bony, S., Meehl, G. A., Senior, C. A., Stevens, B., Stouffer, R. J., & Taylor, K. E. (2016). Overview of the Coupled Model Intercomparison Project Phase 6 (CMIP6) experimental design and organization. *Geoscientific Model Development*, *9*(5), 1937–1958. https://doi.org/10.5194/gmd-9-1937-2016

Flato, G., Marotzke, J., Abiodun, B., Braconnot, P., Chou, S. C., Collins, W., et al. (2013). *Evaluation of climate models, Climate Change 2013 – The Physical Science Basis: Working Group I Contribution to the Fifth Assessment Report of the Intergovernmental Panel on Climate Change* (pp. 741–866). UK: Cambridge University Press. https://doi.org/10.1017/CBO9781107415324.020

Flynn, C. M., & Mauritsen, T. (2020). On the climate sensitivity and historical warming evolution in recent coupled model ensembles. *Atmos. Chem. Phys*, *20*, 7829–7842. https://doi.org/10.5194/acp-20-7829-2020

Fu, H., Liao, J., Yang, J., Wang, L., Song, Z., Huang, X., et al. (2016). The Sunway TaihuLight supercomputer: System and applications. *SCIENCE CHINA Information Sciences*, *59*(7), 072001. https://doi.org/10.1007/s11432-016-5588-7

Gent, P. R., Yeager, S. G., Neale, R. B., Levis, S., & Bailey, D. A. (2010). Improvements in a half degree atmosphere/land version of the CCSM. *Climate Dynamics*, *34*(6), 819–833. https://doi.org/10.1007/s00382-009-0614-8

Gettelman, A., Hannay, C., Bacmeister, J. T., Neale, R. B., Pendergrass, A. G., Danabasoglu, G., et al. (2019). High climate sensitivity in the Community Earth System Model Version 2 (CESM2). *Geophysical Research Letters*, *46*, 8329–8337. https://doi.org/10.1029/2019GL083978

Gettelman, A., Morrison, H., & Ghan, S. J. (2008). A new two-moment bulk stratiform cloud microphysics scheme in the Community Atmosphere Model, Version 3 (CAM3) Part II: Single-Column and Global Results. *Journal of Climate*, *21*(15), 3660–3679. https://doi.org/10.1175/2008JCLI2116.1

Gleckler, P. J., Doutriaux, C., Durack, P. J., Taylor, K. E., Zhang, Y., Williams, D. N., et al. (2016). A more powerful reality test for climate models. *Eos*, *97*. https://doi.org/10.1029/2016EO051663

Golaz, J., Caldwell, P. M., Van Roekel, L. P., Petersen, M. R., Tang, Q., Wolfe, J. D., et al. (2019). The DOE E3SM Coupled Model Version 1: Overview and evaluation at standard resolution. *Journal of Advances in Modeling Earth Systems*, *11*(7), 2089–2129. https://doi.org/10.1029/2018MS001603

Gregory, J. M., Ingram, W. J., Palmer, M. A., Jones, G. S., Stott, P. A., Thorpe, R. B., et al. (2004). A new method for diagnosing radiative forcing and climate sensitivity. *Geophysical Research Letters*, *31*, L03205. https://doi.org/10.1029/2003GL018747

Hogg, A. M. C., Dewar, W. K., Berloff, P., Kravtsov, S., & Hutchinson, D. K. (2009). The effects of mesoscale ocean–atmosphere coupling on the large-scale ocean circulation. *Journal of Climate*, *22*(15), 4066–4082. https://doi.org/10.1175/2009JCLI2629.1

Hourdin, F., Mauritsen, T., Gettelman, A., Golaz, J. C., Balaji, V., Duan, Q., et al. (2017). The art and science of climate model tuning. *Bulletin of the American Meteorological Society*, *98*(3), 589–602. https://doi.org/10.1175/BAMS-D-15-00135.1

Hu, Y., Huang, X., Baker, A. H., Tseng, Y. H., Bryan, F. O., Dennis, J. M., & Yang, G. (2015). Improving the scalability of the ocean barotropic solver in the community earth system model. In *International Conference for High Performance Computing, Networking, Storage and Analysis, SC* (Vol. 15-20-Nove, pp. 1–12). New York, New York, USA: ACM press.

Hu, Y., Huang, X., Wang, X., Fu, H., Xu, S., Ruan, H., et al. (2013). A scalable Barotropic mode solver for the parallel ocean program. In *Lecture notes in computer science (including subseries lecture notes in artificial intelligence and lecture notes in bioinformatics)* (pp. 739–750). https://doi.org/10.1007/978-3-642-40047-6_74

Huang, J., Zhang, X., Zhang, Q., Lin, Y., Hao, M., Luo, Y., et al. (2017). Recently amplified Arctic warming has contributed to a continual global warming trend. *Nature Climate Change*, *7*(12), 875–879. https://doi.org/10.1038/s41558-017-0009-5

Huang, X., Tang, Q., Tseng, Y., Hu, Y., Baker, A. H., Bryan, F. O., et al. (2016). P-CSI v1.0, an accelerated barotropic solver for the high-resolution ocean model component in the Community Earth System Model v2.0. *Geoscientific Model Development*, *9*(11), 4209–4225. https://doi.org/10.5194/gmd-9-4209-2016

Huang, Y., Lu, X., Shi, Z., Lawrence, D., Koven, C. D., Xia, J., et al. (2018). Matrix approach to land carbon cycle modeling: A case study with the Community Land Model. *Global Change Biology*, *24*(3), 1394–1404. https://doi.org/10.1111/gcb.13948

Huang, Y., Zhu, D., Ciais, P., Guenet, B., Huang, Y., Goll, D. S., et al. (2018). Matrix-based sensitivity assessment of soil organic carbon storage: A case study from the ORCHIDEE-MICT model. *Journal of Advances in Modeling Earth Systems*, *10*(8), 1790–1808. https://doi.org/10.1029/2017MS001237

Huffman, G. J., Adler, R. F., Bolvin, D. T., & Gu, G. (2009). Improving the global precipitation record: GPCP Version 2.1. *Geophysical Research Letters*, *36*(17). https://doi.org/10.1029/2009GL040000

Hurrell, J. W., Hack, J. J., Shea, D., Caron, J. M., & Rosinski, J. (2008). A new sea surface temperature and sea ice boundary dataset for the Community Atmosphere Model. *Journal of Climate*, *21*(19), 5145–5153. https://doi.org/10.1175/2008JCLI2292.1

Hurrell, J. W., Holland, M. M., Gent, P. R., Ghan, S., Kay, J. E., Kushner, P. J., et al. (2013). The Community Earth System Model: A framework for collaborative research. *Bulletin of the American Meteorological Society*, *94*(9), 1339–1360. https://doi.org/10.1175/BAMS-D-12-00121.1

Iacono, M. J., Delamere, J. S., Mlawer, E. J., Shephard, M. W., Clough, S. A., & Collins, W. D. (2008). Radiative forcing by long-lived greenhouse gases: Calculations with the AER radiative transfer models. *Journal of Geophysical Research*, *113*, D13103. https://doi.org/10.1029/2008JD009944

IGBP (2000). Global Soil Data Task (IGBP-DIS, ISO-image of CD). International Geosphere-Biosphere Program, PANGAEA. https://doi.org/10.1594/PANGAEA.869912

Jin, Z., Qiao, Y., Wang, Y., Fang, Y., & Yi, W. (2011). A new parameterization of spectral and broadband ocean surface albedo. *Optics Express*, *19*(27), 26,429. https://doi.org/10.1364/OE.19.026429

Kay, J. E., Wall, C., Yettella, V., Medeiros, B., Hannay, C., Caldwell, P., & Bitz, C. (2016). No access global climate impacts of fixing the Southern Ocean shortwave radiation bias in the Community Earth System Model (CESM). *Journal of Climate*, *29*(12), 4617–4636. https://doi.org/10.1175/JCLI-D-15-0358.1

Larson, J., Jacob, R., & Ong, E. (2005). The Model Coupling Toolkit: A new Fortran90 toolkit for building multiphysics parallel coupled models. *The International Journal of High Performance Computing Applications*, *19*(3), 277–292. https://doi.org/10.1177/1094342005056115

Lauritzen, P. H., Bacmeister, J. T., Dubos, T., Lebonnois, S., & Taylor, M. A. (2014). Held-Suarez simulations with the Community Atmosphere Model Spectral Element (CAM-SE) dynamical core: A global axial angular momentum analysis using Eulerian and floating Lagrangian vertical coordinates. *Journal of Advances in Modeling Earth Systems*, *6*(1), 129–140. https://doi.org/10.1002/2013MS000268

Lawrence, D. M., Oleson, K. W., Flanner, M. G., Thornton, P. E., Swenson, S. C., Lawrence, P. J., et al. (2011). Parameterization improvements and functional and structural advances in version 4 of the community land model. *Journal of Advances in Modeling Earth Systems*, *3*(1). https://doi.org/10.1029/2011ms00045

Li, J., & Ramaswamy, V. (1996). Four-stream spherical harmonic expansion approximation for solar radiative transfer. *Journal of the Atmospheric Sciences*, *53*(8), 1174–1186. https://doi.org/10.1175/1520-0469(1996)053<1174:FSSHEA>2.0.CO;2

Liang, Y., Wang, L., Zhang, G. J., & Wu, Q. (2017). Sensitivity test of parameterizations of subgrid-scale orographic form drag in the NCAR CESM1. *Climate Dynamics*, *48*(9–10), 3365–3379. https://doi.org/10.1007/s00382-016-3272-7

Lin, Y., & Colle, B. A. (2011). A new bulk microphysical scheme that includes riming intensity and temperature-dependent ice characteristics. *Monthly Weather Review*, *139*(3), 1013–1035. https://doi.org/10.1175/2010MWR3293.1

Lin, Y., Donner, L. J., & Colle, B. A. (2011). Parameterization of riming intensity and its impact on ice fall speed using ARM data. *Monthly Weather Review*, *139*(3), 1036–1047. https://doi.org/10.1175/2010MWR3299.1

Lin, Y., Dong, W., Zhang, M., Xie, Y., Xue, W., Huang, J, & Luo, Y. (2017). Causes of model dry and warm bias over central U.S. and impact on climate projections. *Natual Communications*, *8*, 881. https://doi.org/10.1038/s41467-017-01040-2

Liu, X., Easter, R. C., Ghan, S. J., Zaveri, R., Rasch, P., Shi, X., et al. (2012). Toward a minimal representation of aerosols in climatemodels: Description and evaluation in the Community Atmosphere Model CAM5. *Geoscientific Model Development*, *5*(3), 709–739. https://doi.org/10.5194/gmd-5-709-2012

Liu, L., Yang, G., Wang, B., Zhang, C., Li, R., Zhang, Z., et al. (2014). C-Coupler1: A Chinese community coupler for Earth system modeling. *Geoscientific Model Development*, *7*(5), 2281–2302. https://doi.org/10.5194/gmd-7-2281-2014

Liu, L., Zhang, C., Li, R., Wang, B., & Yang, G. (2018). C-Coupler2: A flexible and user-friendly community coupler for model coupling and nesting. *Geoscientific Model Development*, *11*(9), 3557–3586. https://doi.org/10.5194/gmd-11-3557-2018

Lu, P., Li, Z. J., Zhang, Z. H., & Dong, X. L. (2008). Aerial observations of floe size distribution in the marginal ice zone of summer Prydz Bay. *Journal of Geophysical Research*, *113*, C02011. https://doi.org/10.1029/2006JC003965

Luo, Y., Ahlström, A., Allison, S. D., Batjes, N. H., Brovkin, V., Carvalhais, N., et al. (2016). Toward more realistic projections of soil carbon dynamics by Earth system models. *Global Biogeochemical Cycles*, *30*(1), 40–56. https://doi.org/10.1002/2015GB005239

Luo, Y., Shi, Z., Lu, X., Xia, J., Liang, J., Jiang, J., et al. (2017). Transient dynamics of terrestrial carbon storage: Mathematical foundation and its applications. *Biogeosciences*, *14*, 145–161. https://doi.org/10.5194/bg-14-145-2017

Luo, Y., Wan, S., Hui, D., & Wallace, L. L. (2001). Acclimatization of soil respiration to warming in a tall grass prairie. *Nature*, *413*(6856), 622–625. https://doi.org/10.1038/35098065

Luo, Y., & Weng, E. (2011). Dynamic disequilibrium of the terrestrial carbon cycle under global change. *Trends in Ecology & Evolution*, *26*(2), 96–104. https://doi.org/10.1016/j.tree.2010.11.003

Luo, Y., White, L. W., Canadell, J. G., DeLucia, E. H., Ellsworth, D. S., Finzi, A., et al. (2003). Sustainability of terrestrial carbon sequestration: A case study in Duke Forest with inversion approach. *Global Biogeochemical Cycles*, *17*(1). https://doi.org/10.1029/2002GB001923

Lüpkes, C., Gryanik, V. M., Hartmann, J., & Andreas, E. L. (2012). A parametrization, based on sea ice morphology, of the neutral atmospheric drag coefficients for weather prediction and climate models. *Journal of Geophysical Research*, *117*, D13112. https://doi.org/10.1029/2012JD017630

Morrison, H., & Gettelman, A. (2008). A new two-moment bulk stratiform cloud microphysics scheme in the Community Atmosphere Model, Version 3 (CAM3) part I: Description and numerical tests. *Journal of Climate*, *21*(15), 3642–3659. https://doi.org/10.1175/2008JCLI2105.1

Myhre, G., Shindell, D., Bréon, F.-M., Collins, W. D., Fuglestvedt, J., & Huang, J. (2013). Anthropogenic and natural radiative forcing. In *Intergovernmental Panel on Climate Change, Climate Change 2013 - the Physical Science Basis* (pp. 659–740). Cambridge: Cambridge University Press. https://doi.org/10.1017/CBO9781107415324.018

Neale, R. B., Gettelman, A., Park, S., Chen, C., Lauritzen, P. H., Williamson, D. L. (2012). *Description of the NCAR Community Atmosphere Model (CAM 5.0). NCAR technical notes*, Ncar/Tn-464+StrBoulder, CO: National Center for Atmospheric Research. Retrieved from. http://www.cesm.ucar.edu/models/cesm1.0/cam/docs/description/cam5_desc.pdf

Neale, R. B., Richter, J. H., & Jochum, M. (2008). The impact of convection on ENSO: From a delayed oscillator to a series of events. *Journal of Climate*, *21*(22), 5904–5924. https://doi.org/10.1175/2008JCLI2244.1

Park, K.-A., Cornillon, P., & Codiga, D. L. (2006). Modification of surface winds near ocean fronts: Effects of Gulf Stream rings on scatterometer (QuikSCAT, NSCAT) wind observations. *Journal of Geophysical Research*, *111*, C03021. https://doi.org/10.1029/2005JC003016

Park, S., & Bretherton, C. S. (2009). The University of Washington shallow convection and moist turbulence schemes and their impact on climate simulations with the Community Atmosphere Model. *Journal of Climate*, *22*(12), 3449–3469. https://doi.org/10.1175/2008JCLI2557.1

Park, S., Bretherton, C. S., & Rasch, P. J. (2014). Integrating cloud processes in the Community Atmosphere Model, Version 5. *Journal of Climate*, *27*(18), 6821–6856. https://doi.org/10.1175/JCLI-D-14-00087.1

Payne, R. E. (1972). Albedo of the sea surface. *Journal of the Atmospheric Sciences*, *29*(5), 959–970. https://doi.org/10.1175/1520-0469(1972)029<0959:AOTSS>2.0.CO;2

Plant, R. S., & Craig, G. C. (2008). A stochastic parameterization for deep convection based on equilibrium statistics. *Journal of the Atmospheric Sciences*, *65*(1), 87–105. https://doi.org/10.1175/2007JAS2263.1

Preisendorfer, R. W., & Mobley, C. D. (1986). Albedos and glitter patterns of a wind-roughened sea surface. *Journal of Physical Oceanography*, *16*(7), 1293–1316. https://doi.org/10.1175/1520-0485(1986)016<1293:AAGPOA>2.0.CO;2

Qin, Y., & Lin, Y. (2018). Alleviated double ITCZ problem in the NCAR CESM1: A new cloud scheme and the working mechanisms. *Journal of Advances in Modeling Earth Systems*, *10*(9), 2318–2332. https://doi.org/10.1029/2018MS001343

Qin, Y., Lin, Y., Xu, S., Ma, H.-Y., & Xie, S. (2018). A diagnostic PDF cloud scheme to improve subtropical low clouds in NCAR Community Atmosphere Model (CAM 5). *Journal of Advances in Modeling Earth Systems*, *10*(2), 320–341. https://doi.org/10.1002/2017MS001095

Rafique, R., Xia, J., Hararuk, O., Leng, G., Asrar, G., & Luo, Y. (2017). Comparing the performance of three land models in global cycle simulations: A detailed structural analysis. *Land Degradation and Development*, *28*(2), 524–533. https://doi.org/10.1002/ldr.2506

Rayner, N. A. (2003). Global analyses of sea surface temperature, sea ice, and night marine air temperature since the late nineteenth century. *Journal of Geophysical Research*, *108*(D14), 4407. https://doi.org/10.1029/2002JD002670

Schmittner, A., & Egbert, G. D. (2014). An improved parameterization of tidal mixing for ocean models. *Geoscientific Model Development*, *7*(1), 211–224. https://doi.org/10.5194/gmd-7-211-2014

Sierra, C. A., & Müller, M. (2015). A general mathematical framework for representing soil organic matter dynamics. *Ecological Monographs*, *85*(4), 505–524. https://doi.org/10.1890/15-0361.1

Small, R. J., DeSzoeke, S. P., Xie, S. P., O'Neill, L., Seo, H., Song, Q., et al. (2008). Air–sea interaction over ocean fronts and eddies. *Dynamics of Atmospheres and Oceans*, *45*(3–4), 274–319. https://doi.org/10.1016/j.dynatmoce.2008.01.001

Smeed, D. A., Mccarthy, G. D., Rayner, D., Moat, B. I., Johns, W., Baringer, M. O., & Meinen, C. S. (2016). *Atlantic meridional overturning circulation observed by the RAPID-MOCHA-WBTS (RAPID-Meridional overturning circulation and Heatflux Array-Western boundary time series) array at 26N from 2004 to 2015*. UK: British Oceanographic Data Centre - Natural Environment Research Council. https://doi.org/10.5285/35784047-9b82-2160-e053-6c86abc0c91b

Smith, R., Jones, P., Briegleb, B., Bryan, F., Danabasoglu, G., Dennis, J., et al. (2010). *The Parallel Ocean Program (POP) reference manual: Ocean component of the Community Climate System Model (CCSM)*. Rep. *LAUR-01853*

Song, X., & Zhang, G. J. (2011). Microphysics parameterization for convective clouds in a global climate model: Description and single-column model tests. *Journal of Geophysical Research*, *116*, D02201. https://doi.org/10.1029/2010JD014833

Song, X., Zhang, G. J., & Li, J.-L. F. (2012). Evaluation of microphysics parameterization for convective clouds in the NCAR Community Atmosphere Model CAM5. *Journal of Climate*, *25*(24), 8568–8590. https://doi.org/10.1175/JCLI-D-11-00563.1

Steele, M., Morley, R., & Ermold, W. (2001). PHC: A global ocean hydrography with a high-quality Arctic Ocean. *Journal of Climate*, *14*(9), 2079–2087.

Stephens, G. L., Li, J., Wild, M., Clayson, C. A., Loeb, N., Kato, S., et al. (2012). An update on Earth's energy balance in light of the latest global observations. *Nature Geoscience*, *5*(10), 691–696. https://doi.org/10.1038/ngeo1580

Stevens, B., Fiedler, S., Kinne, S., Peters, K., Rast, S., Müsse, J., et al. (2017). MACv2-SP: A parameterization of anthropogenic aerosol optical properties and an associated Twomey effect for use in CMIP6. *Geoscientific Model Development*, *10*(1), 433–452. https://doi.org/10.5194/gmd-10-433-2017

Storer, R. L., Zhang, G. J., & Song, X. (2015). Effects of convective microphysics parameterization on large-scale cloud hydrological cycle and radiative budget in tropical and midlatitude convective regions. *Journal of Climate*, *28*(23), 9277–9297. https://doi.org/10.1175/JCLI-D-15-0064.1

Tan, I., Storelvmo, T., & Zelinka, M. D. (2016). Observational constraints on mixed-phase clouds imply higher climate sensitivity. *Science*, *352*(6282), 224–227. https://doi.org/10.1126/science.aad5300

Thomason, L. W. (2012). Toward a combined SAGE II-HALOE aerosol climatology: An evaluation of HALOE version 19 stratospheric aerosol extinction coefficient observations. *Atmospheric Chemistry and Physics*, *12*(17), 8177–8188. https://doi.org/10.5194/acp-12-8177-2012

Tsamados, M., Feltham, D., Petty, A., Schroeder, D., & Flocco, D. (2015). Processes controlling surface, bottom and lateral melt of Arctic Sea ice in a state of the art sea ice model. *Philosophical Transactions of the Royal Society A: Mathematical, Physical and Engineering Sciences*, *373*(2052). https://doi.org/10.1098/rsta.2014.0167

Voldoire, A., Saint-Martin, D., Sénési, S., Decharme, B., Alias, A., Chevallier, M., et al. (2019). Evaluation of CMIP6 DECK experiments with CNRM-CM6-1. *Journal of Advances in Modeling Earth Systems*, *11*(7), 2177–2213. https://doi.org/10.1029/2019MS001683

Wang, Y., Zhang, G. J., & Craig, G. C. (2016). Stochastic convective parameterization improving the simulation of tropical precipitation variability in the NCAR CAM5. *Geophysical Research Letters*, *43*(12), 6612–6619. https://doi.org/10.1002/2016GL069818

Wei, S., Dai, Y., Duan, Q., Liu, B., & Yuan, H. (2014). A global soil data set for earth system modeling. *Journal of Advances in Modeling Earth Systems*, *6*(1), 249–263. https://doi.org/10.1002/2013MS000293

Wild, M., Folini, D., Schär, C., Loeb, N., Dutton, E. G., & König-Langlo, G. (2013). The global energy balance from a surface perspective. *Climate Dynamics*, *40*(11-12), 3107–3134. https://doi.org/10.1007/s00382-012-1569-8

Xia, J., Luo, Y., Wang, Y.-P., & Hararuk, O. (2013). Traceable components of terrestrial carbon storage capacity in biogeochemical models. *Global Change Biology*, *19*(7), 2104–2116. https://doi.org/10.1111/gcb.12172

Xu, F. (2018). Test and evaluation of a simple parameterization to enhance air-sea coupling in a global coupled model. *Satellite Oceanography and Meteorology*, *3*(3). https://doi.org/10.18063/som.v3i3.739

Xu, H., Li, S., Bai, Y., Dong, W., Huang, W., Xu, S., et al. (2019). A collaborative analysis framework for distributed gridded environmental data. *Environmental Modelling and Software*, *111*, 324–339. https://doi.org/10.1016/j.envsoft.2018.09.007

Xu, S., Wang, B., & Liu, J. (2015). On the use of Schwarz–Christoffel conformal mappings to the grid generation for global ocean models. *Geoscientific Model Development*, *8*(10), 3471–3485. https://doi.org/10.5194/gmd-8-3471-2015

Yang, K., Koike, T., Fujii, H., Tamagawa, K., & Hirose, N. (2002). Improvement of surface flux parametrizations with a turbulence-related length. *Quarterly Journal of the Royal Meteorological Society*, *128*(584), 2073–2087. https://doi.org/10.1256/003590002320603548

Yang, K., Koike, T., Ishikawa, H., Kim, J., Li, X., Liu, H., et al. (2008). Turbulent flux transfer over bare-soil surfaces: Characteristics and parameterization. *Journal of Applied Meteorology and Climatology*, *47*(1), 276–290. https://doi.org/10.1175/2007JAMC1547.1

Zadra, A., Williams, K., Frassoni, A., Rixen, M., Adames, Á. F., Berner, J., et al. (2018). Systematic errors in weather and climate models: Nature, origins, and ways forward. *Bulletin of the American Meteorological Society*, *99*(4), ES67–ES70. https://doi.org/10.1175/BAMS-D-17-0287.1

Zelinka, M. D., Myers, T. A., McCoy, D. T., Po-Chedley, S., Caldwell, P. M., Ceppi, P., et al. (2020). Causes of higher climate sensitivity in CMIP6 models. *Geophysical Research Letters*, *47*. https://doi.org/10.1029/2019GL085782

Zeng, X., & Dickinson, R. E. (1998). Effect of surface sublayer on surface skin temperature and fluxes. *Journal of Climate*, *11*(4), 537–550. https://doi.org/10.1175/1520-0442(1998)011<0537:EOSSOS>2.0.CO;2

Zhang, F., & Li, J. (2013). Doubling-adding method for delta-four-stream spherical harmonic expansion approximation in radiative transfer parameterization. *Journal of the Atmospheric Sciences*, *70*(10), 3084–3101. https://doi.org/10.1175/JAS-D-12-0334.1

Zhang, G. J., & McFarlane, N. A. (1995). Sensitivity of climate simulations to the parameterization of cumulus convection in the Canadian climate centre general circulation model. *Atmosphere-Ocean*, *33*(3), 407–446. https://doi.org/10.1080/07055900.1995.9649539

Zhang, H., Wang, Z., Zhang, F., & Jing, X. (2015). Impact of four-stream radiative transfer algorithm on aerosol direct radiative effect and forcing. *International Journal of Climatology*, *35*(14), 4318–4328. https://doi.org/10.1002/joc.4289

Zhang, M., Mariotti, A., Lin, Z., Ramasmamy, V., Lamarque, J., Xie, Z., & Zhu, J. (2018). Coordination to understand and reduce global model biases by U.S. and Chinese institutions. *Bulletin of the American Meteorological Society*, *99*(7), ES109–ES113. https://doi.org/10.1175/BAMS-D-17-0301.1

Zhang, M., Lin, W., Bretherton, C. S., Hack, J. J., & Rasch, P. J. (2003). A modified formulation of fractional stratiform condensation rate in the NCAR Community Atmospheric Model (CAM2). *Journal of Geophysical Research, 108*(D1), 4035. https://doi.org/10.1029/2002JD002523

Zhang, R.-H., Li, Z., Zhu, J., Kang, X., & Min, J. (2014). Impact of tropical instability waves-induced SST forcing on the atmosphere in the tropical Pacific, evaluated using CAM5.1. *Atmospheric Science Letters*, *15*(3), 186–194. https://doi.org/10.1002/asl2.488

Zhao, X., Lin, Y., Peng, Y., Wang, B., Morrison, H., & Gettelman, A. (2017). A single ice approach using varying ice particle properties in global climate model microphysics. *Journal of Advances in Modeling Earth Systems*, *9*(5), 2138–2157. https://doi.org/10.1002/2017MS000952

Zhou, T. J., Chen, Z., Zou, L., Chen, X., Yu, Y., Wang, B., et al. (2020). Development of climate and Earth system models in China: Past achievements and new CMIP6 results. *Journal of Meteorological Research.*, *34*(1), 1–19. https://doi.org/10.1007/s13351-020-9164-0

Zhou, T. J., Zou, L., & Wu, B. (2014). Development of earth/climate system models in China: A review from the Coupled Model Intercomparison Project perspective. *Journal of Meteorological Research*, *28*(5), 762–779. https://doi.org/10.1007/s13351-014-4501-9